

SPARC-GE-04/001
13 July 2004

CONTRIBUTIONS TO EPAC 2004

(5-July 2004, Lucerne, Switzerland)

- 1) Status of the SPARC project
- 2) SPARC Photoinjector Working Point Optimization, Tolerances and Sensitivity to Errors
- 3) Wake Fields Effects in The SPARC Photoinjector
- 4) Emittance Dilution due to 3D Perturbations in RF Photoinjectors
- 5) Laser Temporal Pulse Shaping Experiment for SPARC Photoinjector
- 6) Design Study of a Movable Emittance Meter Device for the SPARC Photoinjector
- 7) An RF Deflector Design for 6D Phase Space Characterization of the SPARC Beam
- 8) The Design of a Prototype RF Compressor for High Brightness Electron Beams
- 9) Design Study for Advanced Acceleration Experiments and Monochromatic X-Ray Production @ SPARC
- 10) An Ultra-High Brightness, High Duty Factor, Superconducting RF Photoinjector

STATUS OF THE SPARC PROJECT*

D.Alesini, S.Bertolucci, M. Bellaveglia, M.E.Biagini, R.Boni, M.Boscolo, M.Castellano, A.Clozza, G.Di Pirro, A.Drago, A.Esposito, M.Ferrario, D. Filippetto, V.Fusco, A.Gallo, A.Ghigo, S.Guiducci, M.Incurvati, C.Ligi, F.Marcellini, M.Migliorati, A.Mostacci, L.Palumbo, L.Pellegrino, M.Preger, R.Ricci, C.Sanelli, M.Serio, F.Sgamma, B.Spataro, A.Stecchi, A.Stella, F.Tazzioli, C.Vaccarezza, M.Vescovi, C.Vicario, INFN-Frascati

F.Alessandria, A.Bacci, I.Boscolo, F.Broggi, S.Cialdi, C.DeMartinis, D.Giove, C.Maroli, V.Petrillo, M.Romè, L.Serafini, INFN-Milano

D.Levi, M.Mattioli, G.Medici, P. Musumeci, INFN-Roma1

A. Cianchi, L.Catani, E.Chiadroni, S.Tazzari, INFN-Roma2

F.Ciocchi, G.Dattoli, A.Doria, F.Flora, G.P.Gallerano, L.Giannessi, E.Giovenale, G.Messina, L.Mezi, P.L.Ottaviani, G. Parisi, L.Picardi, M.Quattromini, A.Renieri, C.Ronsivalle, ENEA-Frascati

S. De Silvestri, M. Nicoli, S. Stagira, Politecnico/Milano

J.B. Rosenzweig, UCLA - Dept. of Physics and Astronomy

D.H. Dowell, P.Emma, C.Limborg, D.Palmer, SLAC

Abstract

The aim of the *SPARC* project is to promote an R&D activity oriented to the development of a high brightness photoinjector to drive SASE-FEL experiments at 500 nm and higher harmonics generation. Proposed by the research institutions ENEA, INFN, CNR with the collaboration of Università di Roma Tor Vergata and INFN-ST, it has been funded in 2003 by the Italian Government with a 3 year time schedule. The machine will be installed at LNF, inside an existing underground bunker. It is comprised of an rf gun driven by a Ti:Sa laser to produce 10-ps flat top pulses on the photocathode, injecting into three SLAC accelerating sections. In this paper we present the status of the design activities of the injector and of the undulator. The first test on the RF deflector prototype and the first experimental achievements of the flat top laser pulse production are also discussed.

INTRODUCTION

The *SPARC* project is an R&D activity to develop a high brightness photoinjector for SASE-FEL experiments funded by the Italian Government in 2003 with a 3 year time schedule. The installation of the machine at LNF will start on September 2004, and the first beam is expected on June 2006. The SPARC [1] complex is composed of an rf gun driven by a Ti:Sa laser producing 10-ps flat top pulses that hit on a photocathode. The out coming beam is injected into three SLAC accelerating

sections to feed a 14 m long undulator, see Fig.1. The main goals of the project are:

(1) the generation of a high brightness electron beam able to drive a self-amplified spontaneous free-electron laser (SASE FEL) experiment in the green visible light and higher harmonics generation,

(2) the development of an ultra-brilliant beam photoinjector needed for the future SASE FEL-based X-ray sources.

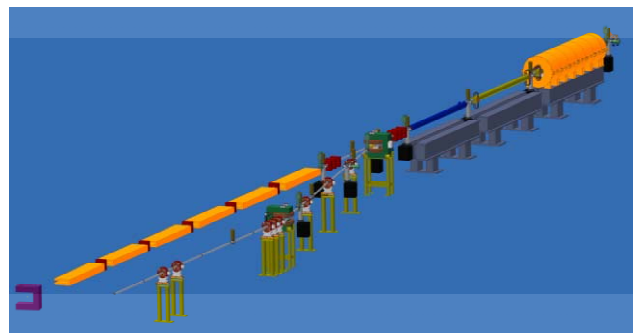


Figure 1.SPARC project layout.

The project is also aiming at the development of sub-ps bunch length diagnostic, at the investigation of the beam emittance degradation due to the CSR in the dogleg magnetic compressor and the effects induced by the surface-roughness wake fields on the beam quality. In the next section of this report the status of the design activities of the injector and undulator is presented. In the

following sections the first test results on the SPARC RF deflector are described and finally those obtained in the flat top laser pulse production are also presented.

SPARC PHOTOINJECTOR WORKING POINT OPTIMIZATION

The beam current required by the FEL experiment pushes the injector design towards the limits of the state-of-the-art for what concerns pulse charge and pulse shape. The design goal of the SPARC accelerator is to provide a 155 MeV bunch with less than 2 μm for the projected emittance and less than 1 μm for the slice emittance. The SPARC FEL operates in the diffraction dominated range and peak current, which, in the range of the diffraction dominated SPARC FEL the beam current is a key parameter for shortening the FEL gain length. Once including possible errors in the undulator system the analysis [2] of the SPARC-FEL operation shows that in order to leave a significant contingency margin to ensure full saturation and testing of harmonic generation a safer parameter set requires a beam having 100 A in 50% of the slices with a slice emittance $\leq 1 \mu\text{m}$. For this purpose a new optimization, with Start-to-End simulations and parametric sensitivity studies aiming to reduce the FEL saturation length, was performed [3].

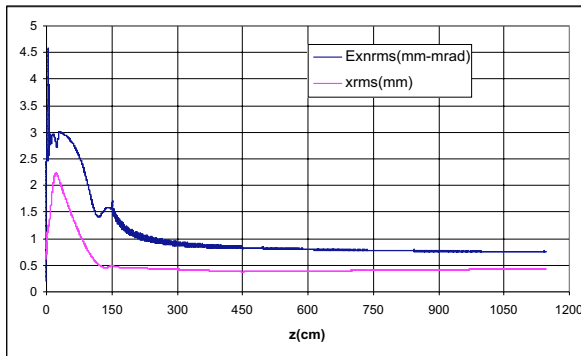


Figure 2: PARMELA computed rms normalized emittance and rms horizontal envelope vs z from gun to the linac output for $Q=1.1 \text{ nC}$, $\tau=10 \text{ psec}$, $\epsilon_{th}=0.34 \mu\text{m}$, laser spot radius= 1.13 mm .

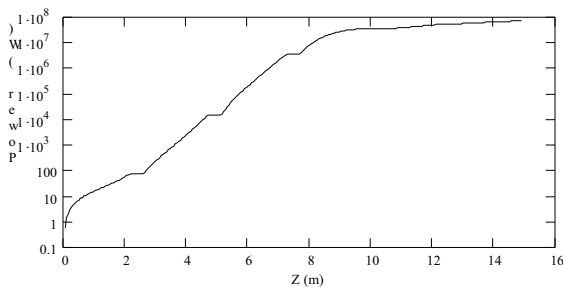


Figure 3: Power vs. z for the SPARC FEL, from GENESIS (final step in STE) simulation. The best result was obtained with a scaling approach [4] in which more charge is launched from the cathode. The configuration that gives the minimum emittance

corresponds to a working point with 1.1 nC and a pulse length of 10 psec. The overall result is the reduction of the FEL-SASE saturation length from 12 to 9 m at 500 nm wavelength, see Fig. 2-3.

Table 1 – Injector Parameters

ELECTRON BEAM	A
Electron Beam Energy (MeV)	155
Bunch charge (nC)	1.1
Repetition rate (Hz)	1-10
Cathode peak field (MV/m)	120
Peak solenoid field @ 0.19 m (T)	0.273
Photocathode spot size (mm, hard edge radius)	1.13
Central RF launch phase (RF deg)	33
Laser pulse duration, flat top (ps)	10
Laser pulse rise time (ps) 10%→90%	1
Bunch energy @ gun exit (MeV)	5.6
Bunch peak current @ linac exit (A)	100
Rms normalized transverse emittance @ linac exit (mm-mrad); includes thermal comp. (0.3)	< 2
Rms slice norm. emittance (300 μm slice)	< 1
Rms longitudinal emittance (deg.keV)	1000
Rms total correlated energy spread (%)	0.2
Rms incorrelated energy spread (%)	0.06
Rms beam spot size @ linac exit (mm)	0.4
Rms bunch length @ linac exit (mm)	1

Table 2 – FEL Parameters

UNDULATOR & FEL	A
Undulator period (cm)	3.0
# Undulator sections	6
Undulator parameter	1.4
Undulator field on axis (T)	
Undulator gap (mm)	11
Undulator section length (m)	2.13
Drifts between undulator sections (m)	0.36
FEL wavelength (nm)	500
Saturation length (m, geometrical)	< 14
FEL pulse length (ps)	8
FEL power @ saturation (MW)	> 80
Brilliance (st. units)	
# Photons/pulse	10^{15}
FEL power @ sat. (MW) 3 rd harm.	> 10
FEL power @ sat. (MW) 5 th harm.	> 0.7

LASER TEMPORAL PULSE SHAPING

The need to minimize nonlinearities in the space charge field of the electron bunch, in particular during the early stages of acceleration from the photo-cathode surface, leads to the needs of shaping the temporal profile of the laser pulse as it strikes the photo-cathode - the required shape is a uniform intensity distribution in time, often termed a flat-top time distribution. Beam dynamics simulations show that flat-top profile should exhibit very sharp edges in the head and tail of the pulse. The associated rise times must be at least shorter than 1 ps, with 0.5 ps being a desirable optimum value

In collaboration with the Milano Politecnico ultra fast laser laboratory, a series of tests have been performed to demonstrate the feasibility of the pulse shaping with the

Dazzler crystal. The preliminary results are of great interest to the SPARC laser pulse shaper design [5].

The obtained temporal intensity was measured by sampling the flat top pulse with the 20 fs reference pulses, delayed varying the optical path length by a translation stage with 100 nm resolution. The very short reference pulse assures a highly precise measurement of the shaped pulse. An interferometric filter was used to reduce the bandwidth of the incoming pulse. The measurements indicated that the acoustic optic crystal could produce pulse with duration up to 12 ps. Figure 4 reports the measurement of shaped intensity profile that approach the required pulse for SPARC photoinjector.

As shown in the plot, the pulse rise and fall time is less than 0.7 ps and the ripple peak to peak is less than 20% and the pulse's duration is thereabouts 11 ps FWHM. These preliminary results are very promising for producing the flat top temporal profile required in the SPARC photoinjector

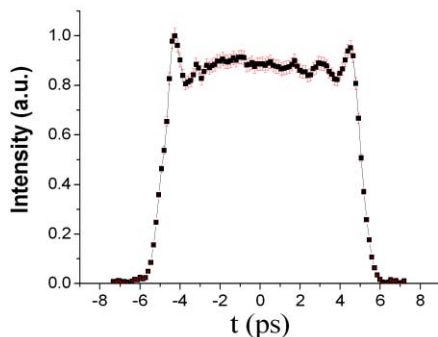


Figure 4: Cross-correlation of the output shaped pulse in double-pass configuration.

RF DEFLECTOR DESIGN & TESTS

The characterization of the longitudinal and transverse phase space of the beam provided by the SPARC photoinjector at 150 MeV is a crucial point to establish the performance quality of the photoinjector itself. By means of an RF deflector it is possible to measure the bunch length: the longitudinal beam distribution can be projected along a transverse coordinate and the image is collected on the screen. Using the orthogonal transverse coordinate distribution, both the horizontal and vertical beam emittances can be measured with the quadrupole scan technique. With the combination of the RF deflector and a dispersive system the longitudinal beam phase space can be completely reconstructed, (flag location FD2). The schematic layout of the measurement is reported in Fig.5. An aluminum cold test model of the 5-cell π -mode rf deflector has been manufactured to LNF specifications and tested (Fig. 6) at the University of Rome "La Sapienza" by members of the SPARC team.

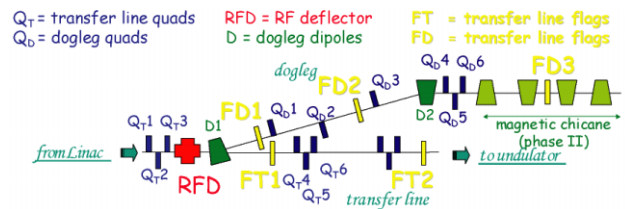


Figure 5: Schematic SPARC measurement layout for high energy beam characterization.

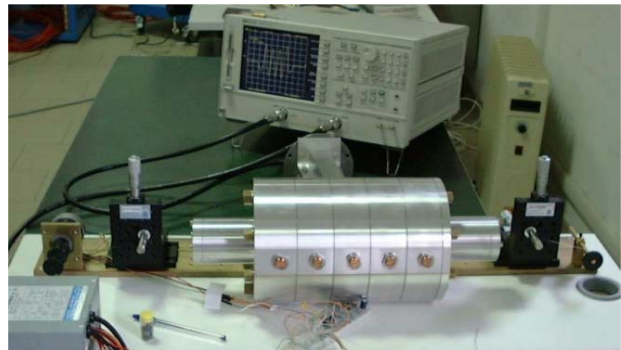


Figure 6: Deflector aluminum prototype and measurement setup.

The results of the bead pull tests on the field profile of the rf deflector π -mode reveal a good level of magnetic field flatness.

CONCLUSIONS

The SPARC project has been approved by the Italian Government and funded in June 2003 with a schedule of three years. After the first year the project has been fully defined, the major components ordered and promising tests on laser pulse shaping with Dazzler and RF deflector for beam diagnostics performed. The installation of the system will start in January 2005.

REFERENCES

- [1] SPARC Project Team, Sparc Injector TDR www.lnf.infn.it/acceleratori/sparc/
- [2] M. Biagini et al., Beam Dynamics Studies for the SPARC Project, Proc of PAC 2003
- [3] M. Ferrario, et al., "SPARC Photoinjector Working Point Optimization, Tolerances and Sensitivity to Errors", these Proceedings
- [4] J.B. Rosenzweig and E. Colby, *Advanced Accelerator Concepts* p. 724 (AIP Conf. Proc. 335, 1995)
- [5] C. Vicario, et al., "Laser Temporal Pulse Shaping Experiment for SPARC photoinjector"
- [6] C. Vaccarezza, et al., "6D Phase Space Characterization of the SPARC Beam"

SPARC PHOTOINJECTOR WORKING POINT OPTIMIZATION, TOLERANCES AND SENSITIVITY TO ERRORS

M. Biagini, M. Boscolo, M. Ferrario, V. Fusco, S. Guiducci, M. Migliorati, C. Sanelli, F. Tazzioli, C. Vaccarezza, INFN-LNF, Frascati (Roma), Italy
 L. Serafini, INFN-MI, Milano, Italy
 L. Giannessi, L. Mezi, M. Quattromini, C. Ronsivalle, ENEA-CR, Frascati (Roma)
 J.B. Rosenzweig, UCLA, Los Angeles (CA), USA

Abstract

A new optimization of the SPARC photo-injector, aiming to reduce the FEL saturation length, is presented together with Start-to-End simulations. A systematic scan of the main parameters around the operating point showed that the probability to get a projected emittance exceeding $1 \mu\text{m}$ is only 10 % and the slice emittance remains below $1 \mu\text{m}$ in all cases.

INTRODUCTION

The SPARC [1] injector will be the first one driving a saturating SASE FEL without the use of a compressor scheme. The FEL requirements in terms of beam current have pushed the design towards the limits of the state-of-the-art for what concerns pulse charge and pulse shape. In order to reach this goal with a good level of confidence we have explored a range of parameters that are not far from the previous best performances obtained in photo-injector laboratories [2]. The design goal of the SPARC accelerator is to provide a 155 MeV bunch with less than $2 \mu\text{m}$ for the projected emittance and less than $1 \mu\text{m}$ for the slice emittance of 50% of slices. Detailed analysis of the SPARC-FEL operation including different errors in the undulator showed that the previous set of beam parameters [3] giving a peak current $I \approx 85 \text{ A}$ does not leave a significant contingency margin to ensure full saturation and testing of harmonic generation in the 14.5 m allocated for the undulator. The peak current, which, in the range of the diffraction dominated SPARC FEL is the key parameter for shortening the FEL gain length, should then be increased. A safer set of parameters requires a beam having 100 A in 50% of the slices with a slice emittance $\leq 1 \mu\text{m}$. For this purpose a new optimization, with Start-to-End simulations and parametric sensitivity studies aiming to reduce the FEL saturation length, was performed. The best performance in terms of increasing final current was obtained with a scaling approach [4] in which more charge is launched from the cathode. The scaling law indicates that the preservation of the beam plasma frequency requires that the spot size be scaled according to $\sigma_x \propto (Q/\sigma_z)^{1/2}$. The configuration that meets the requirement with the minimum emittance corresponds to a working point with 1.1 nC and a pulse length of 10 psec.

START TO END SIMULATIONS

The accelerator consists of a 1.6 cell RF gun operated at S-band with a peak field on the cathode of 120 MV/m and an incorporated metallic photo-cathode followed by an emittance compensating solenoid and three accelerating sections of the SLAC type (S-band, travelling wave), the first one embedded in an array of 13 coils. A transfer line allows the matching with the undulator optics.

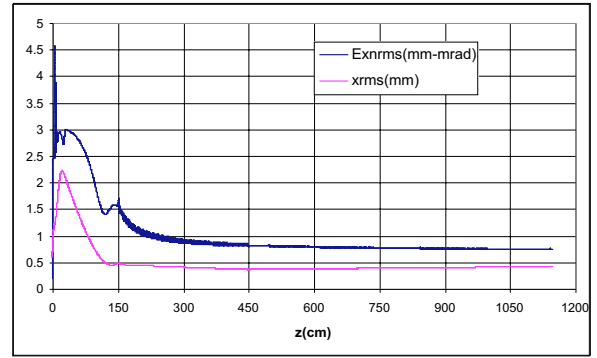


Figure 1: PARMELA computed rms normalized emittance and rms horizontal envelope vs z from gun to the linac output for $Q=1.1 \text{ nC}$, $\tau=10 \text{ psec}$, $\epsilon_{th}=0.34 \mu\text{m}$, laser spot radius= 1.13 mm .

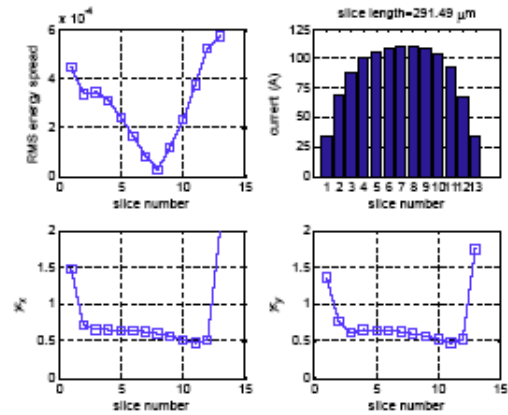


Figure 2: Computed slice parameters: slice energy spread, slice current, x and y rms normalized slice emittance

In Fig. 1 the rms normalised emittance and the rms envelope from the gun to the linac output, as computed by PARMELA [5], are shown for the best case ($\epsilon_n = 0.71 \mu\text{m}$) with increased current ($I=100 \text{ A}$) [6]. In this study, a thermal emittance linearly increasing with the radius and equal to $0.3 \mu\text{m}/1 \text{ mm}$ of radius and a rise time of 1 psec (derived from previous optimization studies) were assumed. It has to be noted that the charge/pulse-length scaling from the parameters found for the original 85 A working point ($\phi_{\text{gun}}=33^\circ$, $B_{\text{sol}}= 2.73 \text{ kG}$, and average longitudinal fields in TW section 1 of $B=750 \text{ G}$, $E=25 \text{ MV/m}$, TW sections 2 and 3 $E=12.5 \text{ MV/m}$) preserves the emittance compensation scheme. The plots of Fig. 2 refer to the slice analysis for the same case: 85% of the particles are in slices with an emittance smaller than $0.7 \mu\text{m}$, 54% have current $\geq 100 \text{ A}$ and 70% have a current $\geq 90 \text{ A}$. In this analysis the slice length has been taken approximately equal to one cooperation length ($\sim 300 \mu\text{m}$).

Two triplets are used to match the optical functions of the beam at linac exit to the values desired at the undulator entrance. This solution, as compared to a doublet and a triplet configuration which was also suitable, has been chosen in order to assure flexibility to the line [7]. In Fig. 3, the rms horizontal beam size from the end of the linac (corresponding to $z=0$ in the plot) to the undulator input is shown. The matching has been performed with MAD [12] including the focal effects of 6 undulator sections interleaved by small horizontally focusing quadrupoles. The effect of each undulator section on the beam has been simulated as a vertically focusing quadrupole.

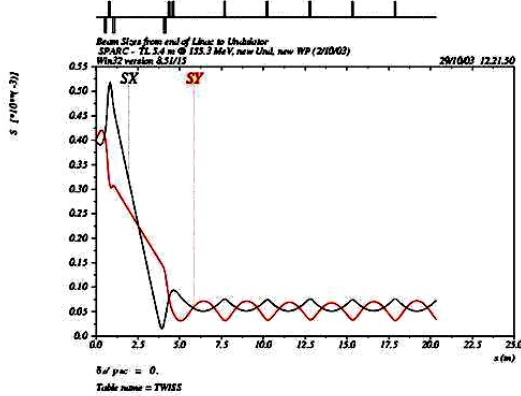


Figure 3: rms beam sizes in mm (black horizontal, red vertical) from the Linac output to the undulator output.

A slice analysis has been carried out in order to evaluate the mismatch of the single slices of the bunch. The relative mismatching parameter:

$$M = 0.5(\beta_o \gamma - 2\alpha_o \alpha + \gamma_o \beta)$$

(α_o , β_o and γ_o being the undulator matched parameters) results to be lower than 1.2 for 85% of the beam.

The undulator parameter set used for the simulation of the SPARC FEL are summarized in Table 1 [8].

Table 1: Undulator parameter set

Period	2.8 cm
# Periods/section	77 (+1 for matching)
Number of Sections	6
K	2.145

The simulation has been performed by using GENESIS 1.3 [9] in time dependent mode, and taking into account the bunch distribution as provided by PARMELA. In Fig.4 the FEL power as a function of z is shown. The saturation length is shorter than 9 m, with a net gain of 2 m compared to the previous optimization.

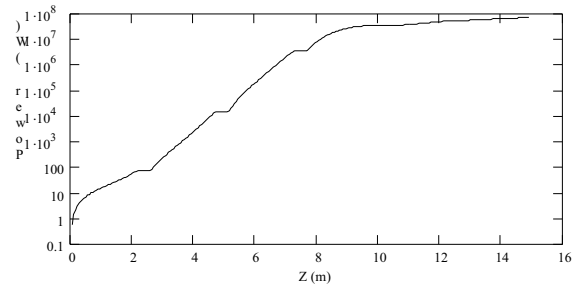


Figure 4: Power vs. z for the SPARC FEL, from GENESIS (final step in STE) simulation

PARAMETER SENSITIVITIES

In order to investigate the stability of the SPARC working point and to predict the most probable values of the projected and slice emittance in realistic conditions, a sensitivity study to various types of random errors in the SPARC accelerator was performed [10]. The study was divided in two steps. In the first one the tolerances of the main tuning parameters were set using the criterion of having a maximum increase of the projected emittance of 10% with respect to the nominal case ($0.71 \mu\text{m}$). In the second step these errors were combined in the defined tolerance ranges and a statistical analysis was performed in order to study the effect of the combination of errors on the projected and slice emittance and on the mismatching at the entrance of the undulator. The sensitivity of the projected emittance to errors of individual parameters that can fluctuate during the machine operation was studied by PARMELA code extensive simulations. The parameters that have been considered are relative to the gun system only and the data were studied at the linac exit.

Table 2: Minimum variation of the single parameters value for a 10% emittance increase

Gun Phase jitter	$\pm 3^\circ$
Charge fluctuation	+ 10%
Gun magnetic field	$\pm 0.4\%$
Gun electric field	$\pm 0.5\%$
Spot radius dimension	$\pm 10\%$
Spot ellipticity	3.5% ($x_{\text{max}}/y_{\text{max}}=1-1.035$)

Step 1: the resulting tolerances on the different tuning parameters are listed in Table 2. It can be seen that the most critical parameters are the electric field amplitude and the spot ellipticity.

Step 2: one hundred PARMELA runs were performed, each one with random error sets within the tolerance limits. PARMELA was interfaced with a MATLAB based program that accepts in input the limits of variation of the single parameters and generates a number of input files in which the six parameters of interest are varied randomly in the pre-defined ranges according with the sampling technique of the “latin hypercube”, an algorithm implemented in the MATLAB statistical toolbox. The numbers used are uniform distributions with average values and rms widths listed in Table 3. The interval of errors distribution is $\pm\sqrt{3} \sigma$ around the average value.

Table 3: Variation of parameters for combined tolerance study of errors in SPARC gun

Parameter	Average value	RMS value
Gun phase	31.5°	1.74°
Charge	1.15 nC	0.032 nC
Gun B field amplitude	2733 gauss	5.8 gauss
Gun E field amplitude	119.9 MV/m	0.32 MV/m
spot radius	1.132	0.068 mm
Ellipticity	1	0.02

The results of the simulations were used to construct the curve plotted in Fig. 5 that gives the probability to obtain an emittance greater or equal than the corresponding value on the abscissa: for example the probability to get a normalized projected emittance $\geq 1 \mu\text{m}$ is less than 10%.

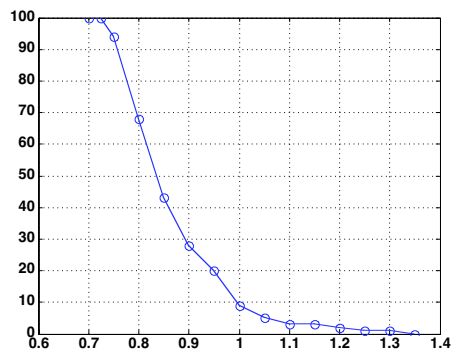


Figure 5: Probability vs emittance over 100 simulations

Concerning the slice emittance, in the 100 simulations it does not exceed $0.9 \mu\text{m}$ for the 9 central slices out of 13 slices, as it can be seen in Fig. 6 in which two extreme cases obtained from the error simulations are compared with the ideal case.

The effect of random errors on the transverse phase space orientation at the entrance of the undulator has also been investigated. The distribution of the average and the rms mismatching factor are respectively 1.3 and 0.32.

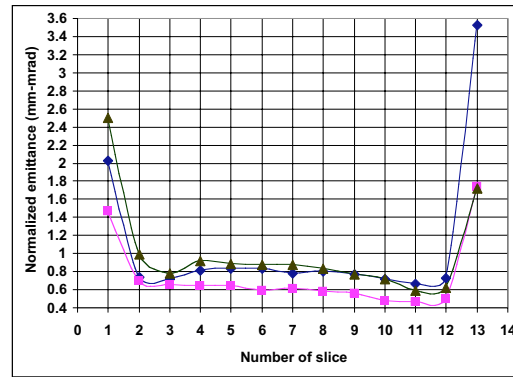


Figure 6: Interval of variation of slice emittance over 100 simulations

CONCLUSIONS

Start-to-End simulations showed that, with a 1.1 nC charge in a 10 ps long bunch we can deliver at the undulator entrance a beam having 100 A in 50% of the slices with a slice emittance $\leq 1 \mu\text{m}$, thus reducing the FEL-SASE saturation length to 9 m at 500 nm wavelength. The stability of the nominal working point and its sensitivity to various types of random errors, under realistic conditions of the SPARC photo-injector operation has also been studied. On this basis it can be concluded that combining multiple errors on tuning parameters the projected and slice emittance values remain within the limits of the SPARC design. Additional systematic investigations taking into account element misalignments, orbit steering and wake fields [11] effects are under way.

REFERENCES

- [1] D. Alesini et al., “Status of the SPARC Project”, this Conference
- [2] J. Yang, J. of Appl. Phys., V. 92, N. 1, (2002)
- [3] M. Biagini et al., Beam Dynamics Studies for the SPARC Project, Proc of PAC 2003
- [4] J.B. Rosenzweig and E. Colby, *Advanced Accelerator Concepts* p. 724 (AIP Conf. Proc. 335, 1995)
- [5] J. Billen, “PARMELA”, LA-UR-96-1835, 1996
- [6] M. Biagini et al., “SPARC injector working point optimisation” SPARC-BD-03/007
- [7] L. Giannessi, L. Mezi, C. Ronsivalle, M. Biagini, M. Migliorati, G. Di Pirro, “SPARC Transfer Line”, SPARC-FEL-03/006
- [8] F. Ciocci, G. Dattoli, L. Riannessi, “SPARC Undulator parameter set”, SPARC-FEL-03/003
- [9] S. Reiche, *Nucl. Instrum. & Meth.* **A429**, 243 (1999)
- [10] C. Ronsivalle, SPARC-BD-03 / 008
- [11] M.Ferrario, V.Fusco, M.Migliorati, L.Palumbo, B.Spataro, “Wake Fields Effects In The Photoinjector of The Sparc Project”, this Conference
- [12] CERN Report CERN/SL/90-13 (AP) (1995)

WAKE FIELDS EFFECTS IN THE SPARC PHOTOINJECTOR

M. Ferrario, V. Fusco[#], B. Spataro, LNF-INFN, Frascati, Italy
M. Migliorati, L. Palumbo, “La Sapienza University”, Roma, Italy

Abstract

When a bunch travels off axis across structures whose shape is not uniform, such as RF cavity or bellows, generates longitudinal and transverse wake fields [1]. In addition transverse time dependent fields (like transverse RF components and wake fields) may induce correlated slice centroids displacement, so that each slice centroid motion is affected also by a different space charge force generated by the next slices. In this paper the analytical diffraction model for wake fields, developed by Bane and Sands has been implemented in the HOMDYN code taking into account also space charge forces acting on the slice centroids.

As a first application, the preliminary evaluation of the emittance degradation in the SPARC linac when structures are misaligned with respect to the nominal axis is reported.

WAKE FIELDS DIFFRACTION MODEL

Single cavity

When the bunch length σ is much smaller then the beam pipe radius a , $\sigma \ll a$, methods of diffraction theory [2] are used to calculate the impedance at high frequencies, $\omega \gg c/a$, where c is the velocity of light.

The model suppose each structure as a pill box cavity, whose geometric dimensions are: a the beam pipe radius, b the cavity radius and g its length. When a bunch reaches the edge of the cavity, the electromagnetic field produced is just the one that would occur when a plane wave passes trough a hole; with this hypothesis it is possible to use the classical diffraction theory of optics to calculate the fields.

According to it, the longitudinal and transverse wake fields, in the high energy regime, are respectively [2]

$$W_{\parallel 0}(s) = \frac{Z_0 c}{\sqrt{2\pi^2 a}} \sqrt{\frac{g}{s}} \quad (1)$$

$$W_{\perp 0}(s) = \frac{2^{3/2} Z_0 c}{\pi^2 a^3} \sqrt{gs} \quad (2)$$

where Z_0 is the characteristic impedance and s the longitudinal coordinate inside the bunch, being $s=0$ the bunch's head.

The above expressions are given for the ultrarelativistic case $\beta \rightarrow 1$; the case of low energy regime was studied in [3-4] where It was shown a dependence of the energy loss and of the wake fields from the relativistic factor γ . However It was shown in [5] that the high energy regime represents an over estimation of the low energy one.

It's worth noting that both the longitudinal and transverse wakes do not depend on the cavity radius b .

Infact part of the diffracted field, generated when the leading edge of the bunch enters the cavity, will propagate in the cavity; if the bunch's rms length σ is shorter than the cavity radius b , then the geometrical condition

$$g < \frac{(b-a)^2}{2\sigma}$$

is verified and the scattered field coming from the upper wall of the cavity will never reach the tail of the bunch itself: this is called “cavity regime”.

Using Eq. 1 and Eq. 2 as a green function we can calculate the transverse and longitudinal wake field:

$$E_{\parallel}^w(s) = \frac{q}{L} \frac{2}{\sqrt{2\pi^2 a \epsilon_0}} \sqrt{\frac{s}{g}}$$

$$E_{\perp}^w(x,s) = \frac{q}{L} \frac{2^{5/2}}{3\pi^2 a^3 \epsilon_0} \frac{s^{3/2}}{\sqrt{g}} x$$

where q and L are the bunch's charge and length respectively.

BEAM DYNAMICS IN HOMDYN

Off-axis beam dynamics

We use the HOMDYN code to study the dynamic of an off axis bunch which travels along structures whose shape is not uniform. The code [6] describes a bunch as a uniformly charged cylinder of charge q and length L , divided in cylindrical slices of radius R_s . The evolution in the time domain of the slice's envelope R_s is described by its envelope differential equation [6] and the centroid longitudinal position z_c of each slice is described by

$$\ddot{z}_c = \begin{cases} \frac{e}{\gamma^3 m} \frac{q}{2\pi \epsilon_0 R_s^2 L \gamma_s} H(\xi_s, R_s, \gamma_s, L) + \\ \frac{e}{\gamma m} E_{\parallel}^w(\xi_s) - \frac{e}{2\gamma m} \left\{ \dot{x}(yB'_z - \sum_i y_{i,off} B'_{z,i}) + \right. \\ \left. - \dot{y}(xB'_z - \sum_i x_{i,off} B'_{z,i}) \right\} \end{cases}$$

where $\xi_s = z_s - z_t$ and z_t is the bunch's tail.

The first term on the right hand side describes the longitudinal space charge on each slice centroid [5], whilst the wake field is the second term on the right hand side. The remaining terms describe the longitudinal motion in a solenoid field; transverse components of the magnetic fields are approximate with the B_z derivative.

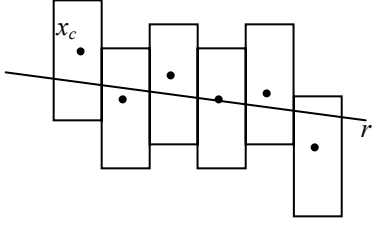


Figure 1: Bunch divided in slices in Homdyn.

In order to describe the displacement of each slice centroid x_c , y_c from the nominal axis of the bunch, it is necessary to include in the code the differential equation describing the centroid motion

$$\ddot{x}_c + \beta\gamma^2 \dot{\beta}\dot{x}_c = \left\{ \begin{array}{l} \frac{e}{\gamma^3 m} \frac{q\gamma}{4\pi\epsilon R_s^2 L} d_{xc} G(\xi, R_s, \gamma, L) + \\ + \frac{e}{\gamma m} \left\{ E_{\perp}^w(x_c^1, \xi_s) + \dot{y}B_z + \right. \\ \left. + \frac{1}{2} \dot{z}(yB'_z - \sum_i y_{i,off} B'_{z,i}) \right\} \end{array} \right.$$

$$\ddot{y}_c + \beta\gamma^2 \dot{\beta}\dot{y}_c = \left\{ \begin{array}{l} \frac{e}{\gamma^3 m} \frac{q\gamma}{4\pi\epsilon R_s^2 L} d_{yc} G(\xi, R_s, \gamma, L) + \\ + \frac{e}{\gamma m} \left\{ E_{\perp}^w(y_c^1, \xi_s) - \dot{x}B_z + \right. \\ \left. - \frac{1}{2} \dot{z}(xB'_z - \sum_i x_{i,off} B'_{z,i}) \right\} \end{array} \right.$$

Each slice's centroid can be transversally displaced from the nominal axis; in this case it experiences a transverse deflection due to the space charge force produced by the neighbour slices (first term on the right hand side) [6] and the transverse wake force (second term on the right hand side). Finally the last terms describe the beam motion in a solenoid field, including the case of solenoid's coils misalignment $x_{i,off}$ and $y_{i,off}$ respect to the nominal axis.

We suppose the transverse wake force on each slice depends on the displacement of the first slice from the axis, x_c^1 or y_c^1 and the space charge on the centroid varies linearly with the distance d_{xc} or d_{yc} of the considered slice's centroid from the straight line r (see Fig. 1). The straight line is obtained interpolating the centroids along the bunch with the least square method.

The space charge on centroids was tested generating a bunch in a case where space charge on centroids is strong; then we compared centroid motion with Parmela results.

Emittance Computation

The total rms emittance is calculated in the code as follow [6]

$$\mathcal{E}_{tot}^2 = (\mathcal{E}_n^{th})^2 + (\mathcal{E}_n^{corr})^2 \quad (3)$$

where \mathcal{E}_n^{th} is the thermal emittance.

When all the slices lies on the same axis, the correlated emittance is only given by the "envelope" emittance

$$(\mathcal{E}_n^e)^2 = \left\langle \frac{X^2}{4} \right\rangle \left\langle \frac{(\beta\gamma X')^2}{4} \right\rangle - \left\langle \frac{X\beta\gamma X'}{4} \right\rangle^2 =$$

$$= \left\langle \frac{a^2}{4} \right\rangle \left\langle \frac{b^2}{4} \right\rangle - \left\langle \frac{ab}{4} \right\rangle^2$$

where X is the slice envelope.

On the contrary if the slices do not lie on the same axis then the correlated emittance is given by the quadratic sum of three terms: the "envelope" emittance mentioned above, the "centroids" and the "cross" emittance, respectively

$$(\mathcal{E}_n^c)^2 = \left\{ \begin{array}{l} \langle (x_c - \langle x_c \rangle)^2 \rangle \langle (\beta\gamma x_c' - \langle \beta\gamma x_c' \rangle)^2 \rangle - \\ - \langle (x_c - \langle x_c \rangle)(\beta\gamma x_c' - \langle \beta\gamma x_c' \rangle) \rangle^2 \end{array} \right.$$

$$= \langle d^2 \rangle \langle e^2 \rangle - \langle de \rangle^2$$

$$(\mathcal{E}_n^{cross})^2 = \left\{ \begin{array}{l} \langle \frac{a^2}{4} \rangle \langle d^2 \rangle + \langle \frac{b^2}{4} \rangle \langle e^2 \rangle + \\ - 2 \langle \frac{ab}{4} \rangle \langle de \rangle \end{array} \right.$$

where $\langle \rangle = \frac{1}{S} \sum_1^S$ is performed over the S slices.

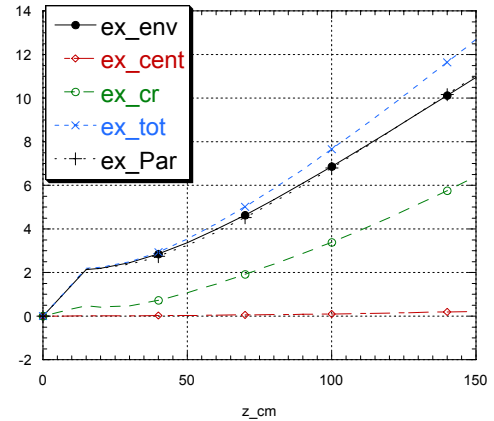


Figure 2: Centroid, cross, envelope and total emittance (light blue line) using Eq. 3, compared with Parmela's emittance results (black crossed line). The bunch is generated with an offset.

The emittance complete expression of an off axis bunch has been inserted in the Homdyn code. Using Parmela's output to obtain slice's envelope and centroid positions, we insert such results in the above equations and calculate analytically the emittance; then we compare the analytical result with the emittance as computed by Parmela. The excellent agreement validates the above computation.

For the Homdyn emittance calculation we assume that the bunch's charge distribution is uniform. The results of

Fig.2 show a good agreement demonstrating the nonlinearities of the space charge force can be neglected.

EMITTANCE DEGRADATION IN THE SPARC PHOTOINJECTOR

We used the improved version of the Homdyn code described in the previous section to preliminary evaluate the emittance degradation at the end of the travelling wave structures (TW) of the SPARC's project [7].

The bunch is generated on axis whilst the TWs can be transversally displaced with respect to the nominal axis; besides the thirteen coils forming the solenoid of the first TW can be independently displaced as well. We looked for the coils' configuration giving the biggest offset of the bunch's centroid from the nominal axis thus enhancing the wake fields across the bunch. We combined it to a worst configuration for the TWs as specified in Table 1.

Table 1: Solenoid coils and TWs misaligned configuration

Device	Δx [mm]	Δy [mm]
Solenoid coil 1	0.	+0.1
Solenoid coils 2-3-4-5-6	+0.1	0.
Solenoid coils 7-8-9-10-11-12-13	0.	-0.1
TW1	0.1	0.1
TW2	-0.1	-0.1
TW3	-0.1	-0.1

Finally we corrected the bunch trajectory inserting three steering coils placed at the entrance of each TW structure.

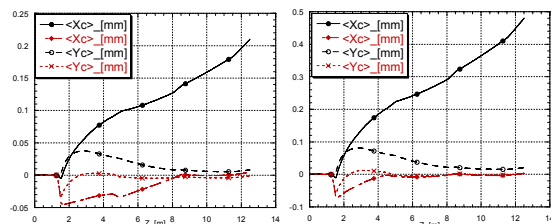


Figure 3: Bunch's centroid position along the structure without (black lines) and with (red lines) steering correction.

Fig.3 shows the bunch centroids positions with and without steerings in the case of the above misaligned configuration for an offset of 0.05mm and 0.1mm. Table2 shows the emittance degradation at the end of the TWs structures whilst Fig.4 shows the emittance behaviour along the structure for the two cases.

It's worth noting the main causes of emittance degradation are the wake fields in the TWs structures. Infact Fig. 5 shows the bunch's emittance when a bunch enters off axis, as an example, in the second TWs structure.

Table 2: Normalized emittance degradation without and with steering correction at the end of the TWs ($z=12.0m$).

Offset	ϵ_{nx} steer off	ϵ_{nx} steer on	ϵ_{ny} steer off	ϵ_{ny} steer on
0.05mm	1.68 μ rad	0.84 μ rad	0.89 μ rad	0.85 μ rad
0.1mm	3.47 μ rad	1.08 μ rad	1.22 μ rad	1.06 μ rad

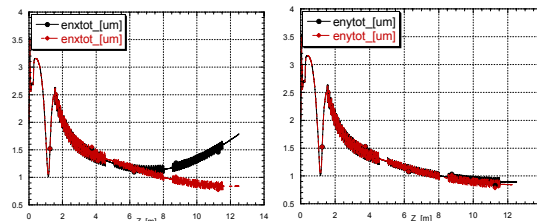


Figure 4: Normalized emittance behaviour along the structure without (black line) and with (red line) steering correction for the case of 0.05mm offset.

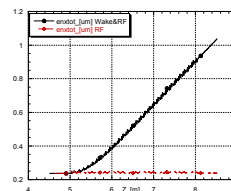


Figure 5: Normalized emittance along the second TW structure for a bunch' offset of 0.1mm when both wake and RF are on (black line) and when only RF is on (red line).

CONCLUSIONS

The analytical diffraction model for wake fields has been implemented in the Homdyn code; we included space charge force acting on each slice's centroids. As a consequence a new analytical calculation for emittance has been developed and inserted in Homdyn. As a first application, a preliminary evaluation of the emittance degradation and tolerances in the SPARC linac when structures are misaligned respect to the nominal axis, has been studied.

ACKNOWLEDGEMENT

The authors would like to thank Concetta Ronsivalle for many helpful and interesting discussions.

REFERENCES

- [1] L. Palumbo et al., "Wake Fields and Impedance", CAS: 5th Advanced Accelerator Physics Course.
- [2] K. Bane, M. Sands, SLAC-Pub-4441
- [3] J.D. Lawson, RHEL/M144.
- [4] E. Keil, NIM 100 (1972) 419-427
- [5] H. Henke, CERN-LEP-RF/85-41
- [6] M. Ferrario et al., SLAC-PUB-8400
- [7] D. Alesini et al., "Status of the SPARC Project", this Conference

EMITTANCE DILUTION DUE TO 3D PERTURBATIONS IN RF PHOTOINJECTORS

M. Quattromini, L. Giannessi, C. Ronsivalle, ENEA, C.R. Frascati (Roma), Italy

Abstract

The predictions from different simulation codes are compared to investigate the effects of fluctuations of quantum efficiency and other sources of in-homogeneities in the performances of a typical RF photoinjector. The layout includes a RF gun and a focusing solenoid in a configuration aimed at minimizing the emittance growth due to space charge effects.

INTRODUCTION

Many applications from X-ray Free electron lasers to high energy colliders require high brightness beams produced by photo-injectors. The final performances of these devices are strictly linked to the beam quality produced by the electron source. In the case of FELs the role played by emittance becomes crucial at sub-nm wavelengths where the emittance is related to the transverse coherence of the output radiation. Most of the emittance budget that characterizes the beam at the undulator is produced at the injector in the first stages of the beam acceleration. The emittance optimization procedure rely on the linear theory [1] which has been verified both experimentally and numerically. In this analysis we examine in these optimized conditions, the role played by a non uniform electron emissivity that may be induced by non-uniformities generated by quantum efficiency variation on photocathode and laser illumination non-uniformity. This study has been performed by using two different codes based on different algorithms: the Los Alamos version of PARMELA (PARMELA-LANL) [2] and TREDI [3]. TREDI has been used in “static” mode, i.e. ignoring effects associated to the finite velocity propagation of signals within the bunch.

PROBLEM DESCRIPTION

The aim of this work is to study the effect of charge in-homogeneities at the cathode surface, by decoupling in a transverse Fourier space, the in-homogeneities occurring at a specific wave-number $k = 2\pi/R$, on a scale of the beam spot radius R , and higher. We have considered a standard S-Band (2856 MHz). 1.6 cells, BNL type photo-injector configuration[4], in a set-up optimized at minimizing the emittance in terms of accelerating gradient, extraction phase, beam spot size, focusing solenoid strength. Space charge effects compensation is achieved assuming both transverse and longitudinal flat charge distribution at extraction. The gun starts at $z=0$ and the drifts ends at $z=2$ m. The

peak electric field in the gun and the solenoid peak magnetic field have been set respectively to 120 MV/m and 2.73 kG. The longitudinal shape of the pulse is square with a length of 10 ps and the charge is 1 nC. The phase of the centre of the bunch is 35° . No thermal emittance is included. The beam spot radius R is 1 mm. The charge distribution extracted from the cathode has been modelled as a perturbation with respect to the ideal case with the following cosine function showing a maximum on the centre of the spot:

$$\rho_p(x, y) = \rho_0 [1 + \delta \cdot \cos(k_n x)] \cdot [1 + \delta \cdot \cos(k_n y)] \quad (1)$$

for $x^2 + y^2 \leq R^2$ and $k_n = n \frac{2\pi}{R}$

Assuming that the values of δ and k_n are small perturbations, we may write in first approximation

$$\varepsilon(k_n, \delta) \cong \varepsilon_0 + \sum_n a_n \sum_j \frac{\delta^j}{j!} \left[\frac{\partial^j}{\partial \delta^j} \varepsilon(k_n, \delta) \right]_{\delta=0} \quad (2)$$

where ε_0 is the value of the unperturbed emittance

and the coefficients $a_n \frac{\partial^j}{\partial \delta^j} \varepsilon(k_n, \delta)$ show the sensitivity of the emittance in this injector configuration to the charge in-homogeneities at the frequency k_n .

The study has been performed by varying the two parameters δ and n and estimating the effect on the normalized rms emittance at the location of the first minimum (fig.1). The parameter δ has been varied with values comprised between 0 and 40% and n the values $n = 1/2, 1, 2, 4$.

A previous comparison between the two codes in the ideal configuration, i.e. at $\delta=0$, has shown a good agreement [5]. A final remark is in order about phase-space random generation: results obtained by Monte Carlo simulations of such low-emittance beams are very sensitive to the initial values of macro-particles used to describe the macroscopic charge distribution. As a matter of fact, the fluctuations associated with standard pseudo-random numbers generators translate in charge density gradients and fields obfuscating the emittance compensation mechanism at work. As a consequence, less than linear convergence is achieved as a function of the number of macro-particles. Quasi-random (or Halton or Sobol[6]) sequences yield usually much faster convergence because of the highly desirable capability of uniformly populating a given n -

dimensional box. This prevents macro-particles from getting too close one another, which induces a spurious collisional regime and unphysical space charge fields. For the study presented here, the quasi-random generator has been slightly modified by using the rejection method [6] to fit the distribution (1). The phase spaces were generated by TREDI and the particles set has been exported to PARMELA to ensure exactly the same initial conditions.

CALCULATIONS RESULTS

The behaviour of the transverse emittance as a function of the longitudinal coordinate at $\delta=40\%$, for different values of k_n is shown in fig. 1 as computed by PARMELA. The emittance undergoes a typical series of oscillations due to the changes in correlation between longitudinal slices along the bunch which are subject to different focusing as a function of the extraction phase. These oscillations exhibit the well known structure with a double minimum located at the places where the correlation is maximized. In the figure the effect of distributions with $n \neq 0$ on emittance is visible and compared to the optimal conditions.

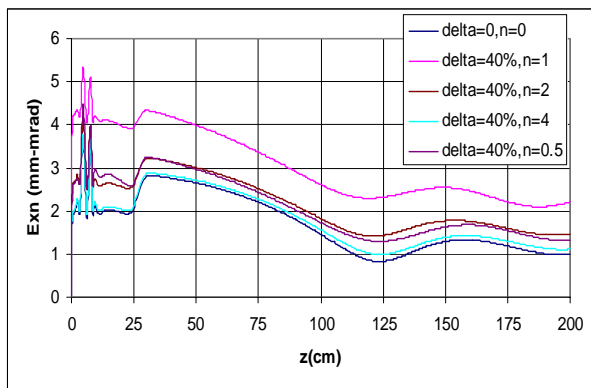


Fig.1 RMS horizontal normalized emittance vs z for $\delta=40\%$ and $n=1/2, 1, 2, 4$ compared with the uniform case

As an indication of the emittance of the beam we have considered the first minimum, whose position may depend on the in-homogeneity parameter δ especially at the lower perturbation frequencies k_n . In figure 2 the value computed by PARMELA of the horizontal normalized rms emittance divided by the value obtained with a completely uniform distribution is plotted as a function of n . A qualitatively similar behaviour has been obtained with TREDI as it is shown in figure 3 where TREDI and PARMELA results relative to the emittance growth for $\delta=20\%$ are compared.

For $n=1/2$ TREDI indicates a reduction of the emittance not evidenced by PARMELA, but for values of $n \geq 1$ the two codes are in fairly good agreement and both give the maximum emittance increase for $n=1$,

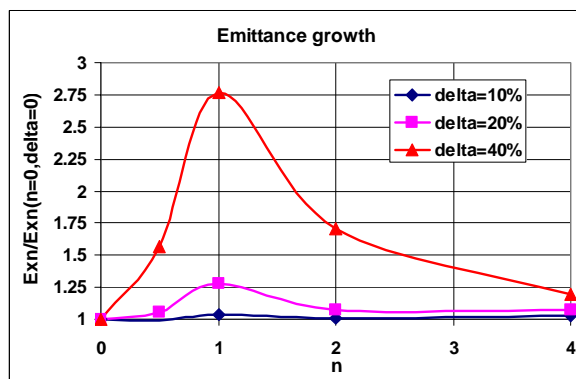


Figure 2: Emittance growth vs n in the position of the first minimum of the emittance as computed by PARMELA

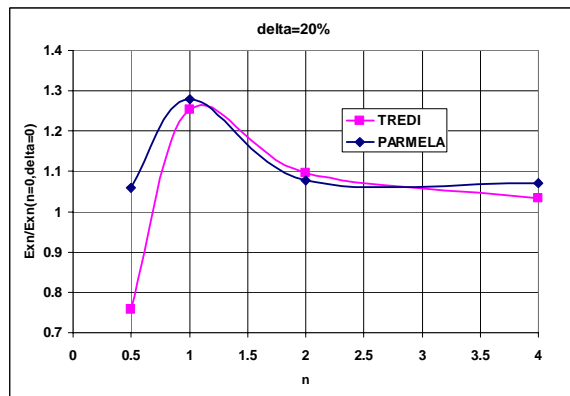


Figure 3: Emittance growth vs n in the first emittance minimum for $\delta=20\%$ as computed by PARMELA and TREDI

This behaviour may be understood by looking at the x - y space shown in fig.4. in three longitudinal positions: at the cathode ($z=0$), near the minimum of emittance ($z=1.25$ m) and near the maximum of emittance ($z=1.5$ m). The non-linear space charge forces induced by the non uniform transverse distribution at the cathode gives a deformation of the beam shape. The distortion is stronger when the non-uniformities are more localized respect to the cases in which they are more diffused and tend to a partial re-compensation along the drift.

In fig 4 the action of the solenoid focusing is also visible as a rotation of the distribution around the axis.

The emittance degradation increases with the modulation depth δ as expected. An analysis of the data has shown a repeatable dependence of the emittance growth with δ of the following functional form,

$$\mathcal{E}(\delta, k_n) = \varepsilon_0 (1 + a_n \delta^3)$$

suggesting that the first two coefficients of the series expansion (2) are negligible. In table 1 the values of the coefficients derived from the analysis of TREDI and PARMELA data are reported.

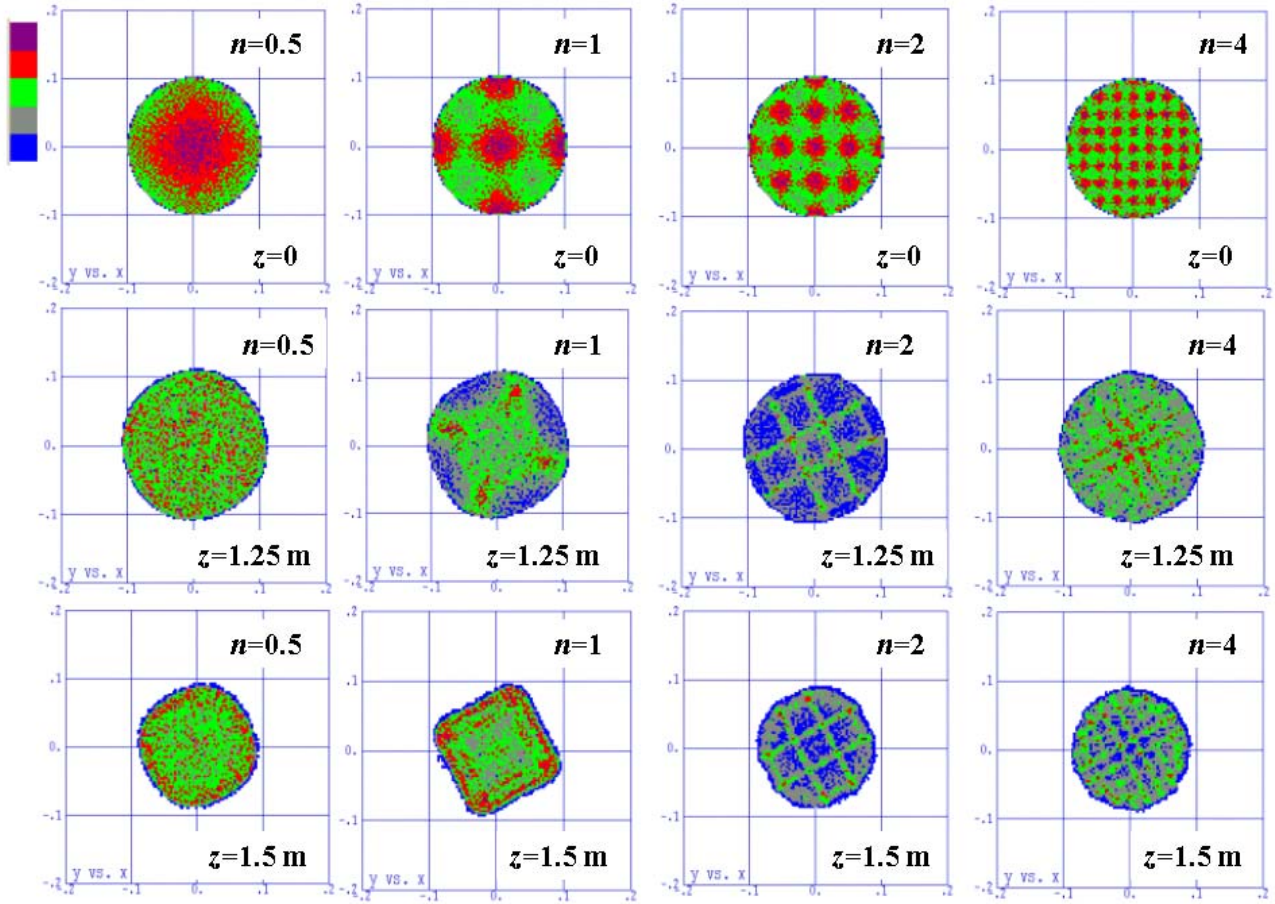


Figure 4: X-Y plots derived from PARMELA computations for $\delta=20\%$ in different longitudinal positions

Table 1: coefficients a_n

Coefficient	TREDI	PARMELA
a_1	21	27
a_2	12	11.5
a_4	3.3	3

CONCLUSIONS

The preliminary analysis presented in this paper has been based on the observation of the projected emittance at the location of the first minimum along the propagation, as a function of the frequencies associated to the cosine perturbation defined in (1). A scaling law of this effect in function of the perturbation amplitude has been derived and some indications of the dependence of the effect with the transverse frequency have been obtained. In the future we plan to have further verifications of these scaling laws by extending the analysis to sine-like perturbations and to higher transverse oscillation frequencies. While with the sine-like perturbation we might expect similar results at high frequencies k_n , the situation might be substantially different at low n where the phase has a significant

influence on the distribution symmetry. Furthermore we plan to continue this study by extending the observation to the beam slice emittance, which is not affected by correlations between slices and is probably a better indicator of the influence of cathode inhomogeneities on the beam quality. This work will require a significant computational effort since the number of macroparticles and the transverse mesh fineness for the evaluation of the fields grow non-linearly with the frequency associated to the transverse mode.

REFERENCES

- [1] L. Serafini, J.B. Rosenzweig "Envelope analysis of intense relativistic quasilaminar beams in RF photoinjectors: a theory of emittance compensation" Phys. Rev. E55 (1997) p.7565
- [2] L. Young, J. Billen "PARMELA" LA-UR-96-1835
- [3] L. Giannessi, M. Quattromini, PRST-AB 6 120101 (2003), Web site: <http://www.tredi.enea.it>
- [4] LCLS Design Report, SLAC-R-593, April 2002
- [5] C. Limborg et al. "Code comparison for simulations of photo-injectors ". Proceedings PAC2003
- [6] Numerical Recipes in C: The Art of Scientific Computing , W.H. Press et al., Cambridge Univ. Press, Cambridge UK, 2nd ed. (1992), p. 311 ff.

LASER TEMPORAL PULSE SHAPING EXPERIMENT FOR SPARC PHOTOINJECTOR

C. Vicario[#], A. Ghigo, INFN-LNF, Frascati, Rome, Italy
M. Petrarca, Univ. La Sapienza, Rome, Italy
I Boscolo, S. Cialdi, A Flacco INFN, Milan Italy
M. Nisoli, G. Sansone, S. Stagira, Politecnico, Milan, Italy
C. Vozzi, University of Milan Italy.

Abstract

Laser for driving high brightness photoinjector have to produce UV square pulse which is predicted to be the optimum profile for emittance compensation in advanced photoinjectors. The longitudinal laser pulse distribution, according to numerical simulations for the SPARC photoinjector, must be square with rise and fall time shorter than 1 ps and flat top variable up to 10 ps FWHM. In this paper we report the results of pulse shaping obtained using an acousto-optic (AO) programmable dispersive filter (DAZZLER). The DAZZLER was used to perform spectral amplitude and phase modulation of the incoming 100 fs Ti:Sapphire pulses. Because of the finite length of the crystal the maximum duration of the shaped pulse is 6 ps. To overcome this limitation we used a configuration in which the laser pulses pass twice through the AO filter. A dispersive glass section was also used to lengthen the pulse with a single pass in the DAZZLER. In this paper we report the experimental setup, hardware description and time and frequency domain measurements.

INTRODUCTION

The SPARC project (Sorgente Pulsata Autoamplificata di Radiazione Coerente) is a 150-MeV advanced photoinjector designed to drive a SASE-FEL in the visible and near UV range[1]. The machine consists of a Ti:Sa laser to illuminate a metal photocathode, an high gradient rf-gun and 3 SLAC s-band accelerating sections. The photoinjector, which is under construction at LNF, is conceived to explore the emittance correction technique and high current production, with proper preservation of the transverse emittance. The aim of the project is to explore the scientific and technological issues for the construction of SASE-FEL based X-ray source.

The photocathode drive lasers for high brightness electron beam applications must show very specific capabilities motivated by two major considerations: the low photo-emission efficiency of robust photocathodes requires high UV energy to extract the needed charge; the emittance compensation process is most successful with uniform temporal and spatial laser energy distribution. In particular beam dynamics simulations confirm that the optimal pulse shape has flat-top profile up to 10 ps, with ripple less than 30% and very sharp edges of the pulse:

the rise and fall times must be at least shorter than 1 ps. To assure repeatable SASE-FEL performance, additional demands are low energy fluctuations (<5%), small time jitters from pulse-to-pulse (<1 ps) and good pointing stability. Finally, the laser pulses have to be synchronized with the accelerator master oscillator, in order to extract electrons at a precise phase of the RF field. To satisfy all these requirements it is necessary a pulse shaper device and a large bandwidth laser system; so the Ti:Sa technology was adopted. In Fig. 1 is reported the laser layout for SPARC.

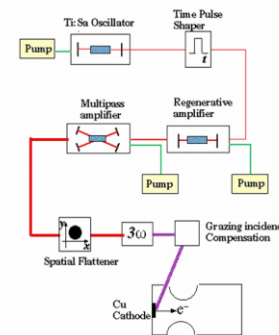


Figure 1: Conceptual layout of SPARC laser system.

The 100 fs pulses delivered by Ti:Sa laser naturally display a sech^2 temporal profile. The device that convert this pulse shape in a flat top one works as a spectral filter. The pulse shaper has high insertion losses and low damage thresholds: therefore the filtering has to be applied before amplifying the laser pulse. Beside, the spectral manipulation has to retain almost all the spectrum of the incoming pulse because otherwise it would induce problems for the amplification process [2].

To produce the desired pulse shape it was proposed a liquid crystal matrix placed between two gratings [3]. The liquid crystal mask can operate as spectral amplitude filter or phase shifter.

Instead we tested a new technique based on a programmable AO dispersive filter produced by FASTLITE (named DAZZLER). This device is able to perform simultaneously amplitude and phase modulation.

Because of the filter behavior of the DAZZLER the output signal in the spectral domain is given by [4]:

[#]carlo.vicario@lnf.infn.it

$$S_2(\omega_2) = S_1(\omega_1) \cdot S_{ac}(\omega_{ac}) \quad (1)$$

where S_2 , S_1 and S_{ac} are respectively the complex output optical signal, the input signal and the acoustic transfer function.

In details inside the AO filter, a chirped acoustic wave and the optic pulse linear polarized along the ordinary axis interact in a TeO_2 crystal. The AO interaction occurs for different optical wavelengths, at different depths, where the AO phase matching condition is satisfied [5]. The interaction induces a rotation of the polarization toward the extraordinary axis. The refraction index along the extraordinary axis is different from that along the ordinary one and thus a frequency dependent phase delay is obtained. In practice the filter shifts in time the pulse frequencies thus stretching the pulse temporally. The intensity of the acoustic signal governs the amplitude modulation of the optical wavelengths. A radio frequency generator (with frequencies between 40 and 55 MHz) drives a piezo-transducer to produce the acoustic wave in the crystal.

EXPERIMENT OVERVIEW

We tested the DAZZLER at the ULTRAS laboratory of the Politecnico in Milan.

The source used for the experiment was an amplified Ti:Sapphire laser similar to the one expected for SPARC. The laser delivered 20 fs FWHM, 1 mJ pulses at 1 kHz repetition rate with the central wavelength at 800 nm, in horizontal linear polarization. A small fraction of the laser beam (20 μJ) was sent to the experimental setup; here the beam was divided in two arms by a 50% beam splitter.

In the first arm the beam was sent through a 10-nm band pass spectral filter, to obtain 100 fs FWHM pulses (as we expect for the SPARC laser), and then through the DAZZLER crystal. The second pulse (gate pulse) was sent to a delay line controlled by a 100 nm linear resolution stepper motor. For the measurement the shaped pulse and the gate signal overlapped in a non linear BBO crystal. The emerging double frequency pulse was proportional to the cross-correlation of the two pulses, and was measured by a photodiode. The measurement was based on the lock-in technique.

The cross-correlation corresponded in our case to the temporal intensity measurement of the shaped pulses, because the gate pulse was much shorter than the DAZZLER pulse. The resolution was about the duration of the gate optical signal (20 fs).

We developed the numerical code, in Labview environment, to simulate the optimal phase and amplitude modulation for the DAZZLER. The calculation allowed the control of the shaping in real time according to Eq. 1. The program simulates the behavior of the DAZZLER: it allows the modification of the amplitude and the spectral phase of the measured input spectrum, and then, through the FFT, calculate the output temporal profile. With the amplitude modulation we corrected also the non flat response of the DAZZLER due to the frequency-dependent diffraction efficiency. A general comment is

that we cannot impose the spectral modulation as sinc function which would give under Fourier Transform a perfect square profile in time. This is because the output pulse would have a too narrow spectral bandwidth, not compatible with Ti:Sa amplifier operation[2].

Because of the finite length of the crystal (2.5 cm) the maximum theoretical duration of the shaped pulse is 6 ps. To overcome this limitation we used a configuration in which the laser pulses pass twice through the AO filter. In this case we observed high energy losses ($\approx 80\%$). For this reasons we tested also a configuration with a single pass through the DAZZLER crystal and through 30 cm of dispersive glass (SF57). The glass introduced an extra second order phase modulation. The total dispersion of the glass sections was 0.2 ps². In this way the losses were reduced to 50%. The single passage simplified also the alignment of the AO crystal.

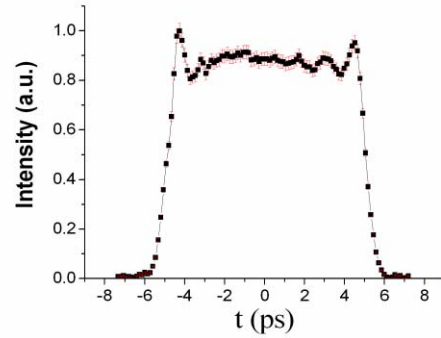


Figure 2: Cross-correlation of the output shaped pulse in double-pass configuration.

In Fig. 2 is reported the cross-correlation signal obtained with double passage configuration, with the estimated error bars. The measured pulse shows a very sharp rise and fall time, definitely less than 1 ps, and the pulse duration is about 10 ps FWHM. The ripple on the top of the pulse is very smoothed. The overshoots remains below 15% of the average value of the pulse intensity. The pulse's characteristics obtained are in good agreement with the SPARC requests for the pulse [6].

In Fig. 3 it is shown the input spectral intensity, the phase and amplitude modulation used to obtain the flat top pulse reported in Fig. 2.

The phase modulation is given by symmetric polynomial expansion up to 8th order centered at 780 nm. The amplitude modulation (absolute value of the transfer function) is given by Eq. 1 assuming a Super-Gaussian output amplitude spectrum:

$$|S_2| = \text{Exp} \left[- \left(\frac{|v - v_0|}{\Delta v} \right)^n \right] \quad (2)$$

with the exponent $n=9.35$, bandwidth $\Delta v=4.14$ THz and v_0 is the central frequency. It is important to stress the fact that we did not impose the DAZZLER a phase curve which gives the same group delay (defined as the derivative of the phase respect to the frequency) for two different frequencies. This in fact could have very

deleterious consequences including unstable beat phenomena.

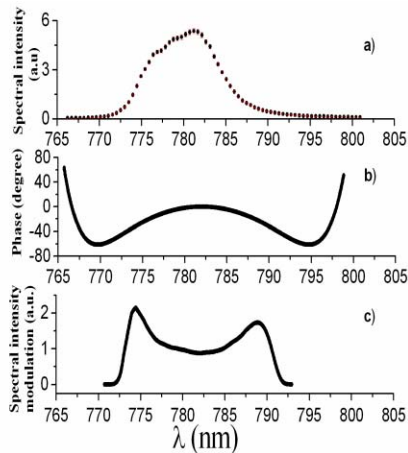


Figure 3: (a) input spectrum; (b) phase modulation; (c) amplitude modulation.

In Fig. 4 is reported the cross-correlation signal with the estimated error bars, obtained with single passage through the AO crystal and the dispersive glass. In this case the rise and fall time is more smooth than the double passage results.

The reason is that in this configuration the DAZZLER dynamics is reduced and the glass introduce only second order phase shift without high orders which are responsible for the rise and fall time duration. Thus we have a lower ripples as the Gibbs phenomenon asserts. However the result still satisfies the SPARC requirements. The duration of the shaped pulse is about 6.5 ps; if a longer temporal pulse duration is requested, it is necessary the insertion of additional dispersive glass.

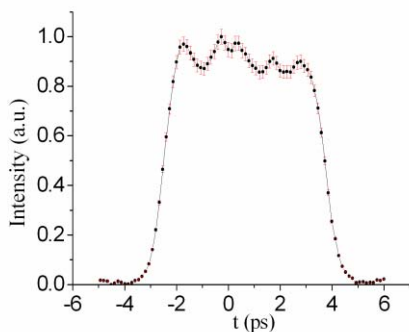


Figure 4: Cross-correlation of the shaped pulse in single-pass configuration.

The best results were obtained with a feedback from cross-correlation measurements and by successive optimizations of the filter's parameters. The cycle went on until we found the best result achievable. For further improvements we think it will be helpful to develop a genetic algorithm with an automatic feedback loop.

The results were reproducible with not appreciable differences, over a time scale compatible with the laser source stability. We observed also a very low influence by beam pointing instability of few mrad. This value is much larger than the typical Ti:Sa oscillator performances. Finally measurements showed that the DAZZLER filter is insensitive to microseconds jitters between acoustic wave and laser pulses.

In the SPARC laser layout the Dazzler is placed ahead of the laser amplifier, therefore the final temporal profile of the pulse on the cathode is determined by the successive processes that the pulse undergoes. The effects of amplification, UV conversion and propagation through the optical transfer line are to be investigated. However the flexibility of the DAZZLER device could also be used to compensate some of these effects. To integrate the DAZZLER in the whole laser system it is required the development of temporal UV diagnostic tools.

OUTLOOK

The experiment conducted was conceived as a proof of the flat top pulse generation by AO crystal.

The preliminary measurements conducted indicate the DAZZLER as a promising technique to produce the required flat top laser pulses up to 10 ps FWHM in double passage configuration. We believe also that, in the single passage configuration, it is possible to obtain longer pulse up to 10 ps with more external dispersion.

We think that better temporal profile can be achieved with a more careful control of the acoustic modulation; this task can be accomplished by improving the control code via genetic algorithm. More work should be devoted to the integration of the DAZZLER with the whole photo-injector laser system and optical diagnostics.

REFERENCES

- [1] D. Alesini et al. An R&D program for a high brightness electron source at LNF, Proceeding EPAC, Paris 2002, pag. 1807-1809.
- [2] P. Maine et al. IEEE J. Quantum Electronics 24 (1988) 398.
- [3] A. M. Wiener, D. E. Leaird, J. S. Patel and J. R. Wullert *Opt. Lett.* **15**, 326 (1990).
- [4] P. Tournois, *Optics Communication* 140 (1997) 245.
- [5] A. Yariv, P. Yeh, *Optical Wave in Crystals*, Wiley, New York 1984.
- [6] L. Palumbo et al. Technical Design Report for the SPARC Advanced Photo-Injector, Preprint INFN-LNF, 12-1-2004.

DESIGN STUDY OF A MOVABLE EMITTANCE METER DEVICE FOR THE SPARC PHOTOINJECTOR

A. Cianchi[#], L. Catani, INFN-RM2, 00133 Roma (Italy)

M. Boscolo, M. Castellano, A. Clozza, G. Di Pirro, M. Ferrario, D. Filippetto, V. Fusco, INFN-LNF, 00044 Frascati (Italy)

L. Giannessi, L. Picardi, M. Quattromini, C. Ronsivalle, C.R. Frascati ENEA 00044 Frascati (Italy)

Abstract

Preliminary studies of the SPARC RF-Gun are planned to obtain an accurate analysis and optimization of the emittance compensation scheme, measuring the beam emittance evolution downstream the RF-Gun with an appropriate diagnostic system. Since in a space charge dominated beam the use of the quad-scan method is not applicable a 1D pepper-pot method will be used instead. A metallic mask with narrow slits will be installed on a longitudinally movable support, spanning a 1.5 m long region, to measure the emittance in several positions and reconstruct its evolution in the post gun section. Numerical simulations of the measurement, mainly based on PARMELA, have been used to estimate the achievable accuracy and to optimize the experimental setup. Wake field effects induced by the beam propagation through the long bellows have been also investigated with HOMDYN. Based on these simulations the design of the apparatus, called emittance-meter, has been realized and is under construction at LNF.

INTRODUCTION

The aim of the SPARC project is to promote an R&D activity to develop a high brightness photo-injector suited to drive a SASE-FEL experiment.

The first phase of the SPARC Project foresees the systematic emittance measurement along the post-RF gun drift where the emittance compensation process occurs. The complete characterization of the beam parameters at different distances from the cathode is important for code validation and to place the first accelerator module in the best position according to the emittance compensation scheme.

For this measurement a dedicated movable (in z) emittance measurement tool will be used giving the possibility to perform measurements from about $z=83$ cm to $z=233$ cm (the cathode is at $z=0$). The technique that will be employed for the emittance measurement consists in the use of a double system of emittance slit-arrays, horizontal and vertical, to measure the emittance and the Twiss parameters in both planes.

Numerical simulations of measurement based on this apparatus, mainly using ad-hoc simulation codes and PARMELA beam dynamics calculation, have been done [2] in order to optimize the mechanical design and the overall system performances.

THE EMITTANCE-METER

General Layout

The technique that will be employed for the emittance measurement consists in selecting one or several beamlets by means of an intercepting multi-slit mask (fig.1) or a single slit moving transversally over the beam spot.

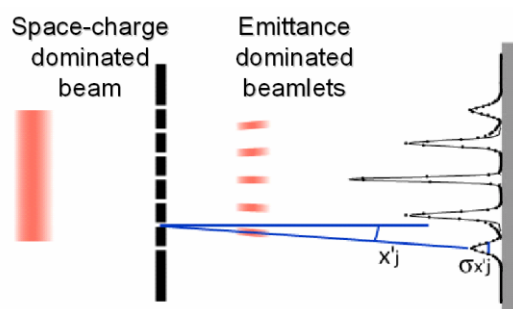


Figure 1: Multi-slits mask intercepting a space charge dominated beam.

The slits reduce the dominated space charge incoming beam into some emittance-dominated beamlets that drift up to an intercepting screen. If the screen response is linear, the intensity of beamlets spots on the screen are directly proportional to the number of particles in the beamlets which hit the screen and the rms un-normalized emittance value can be retrieved by the formula [1].

The slits mask must stop, or largely degrade, the intercepted components of the beam. High-Z material, 2 mm thick tungsten in our case, will be used. The design of the apparatus is sketched in Fig.2. Two 1.5 m long bellows allow the cross, housing the slits mask, to be moved along a region where the most relevant part of the emittance compensation process occurs.

The measurement conditions change at different longitudinal positions, as consequence the distance between the slits mask and the analyzing screen cannot be fixed. For instance, when the value of the Twiss parameter α is close to zero (beam is highly collimated) a long drift is needed to produce a noticeable difference in the beamlets size respect to the slits width. On the opposite when the beam is strongly diverging a long drift is unadvisable because the beamlets spread on a large area. In this case the possible beamlets overlapping and the lower signal-to-noise ratio might reduce the accuracy of the measurement. For this reason another bellow is foreseen between the slits mask and the screen, allowing

[#]cianchi@roma2.infn.it

changing their distance from 20 to 40 cm, a measure that the simulations demonstrated to be a good compromise for the different scenarios.

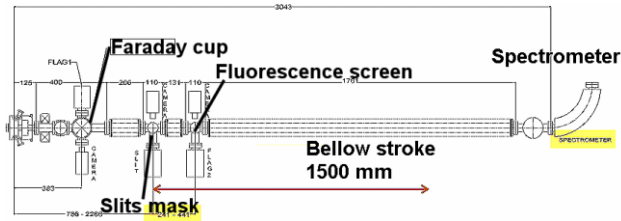


Figure 2: Emittance-meter design.

The beam will be spent in a dump after a bending magnet. Before the dump, beam energy and energy spread will be measured.

Slits Mask

Two slit masks, mounted on two independent holders 90° with respect to each other, will be used to measure the emittance in the horizontal and vertical planes. A 2 mm thick tungsten mask was considered as sufficient to completely stop the 5.6 MeV electron beam. The slits width will be $50 \mu\text{m}$, being it a compromise between the requirement to produce emittance dominated beamlets, so the space charge contribution is negligible after the mask, and the practical requirement to have still enough electrons for the sensitivity of the analysis system. PAMELA code was run with 450K particles to check the influence of the residual space charge and, as evident from Fig.3, the contribution is negligible.

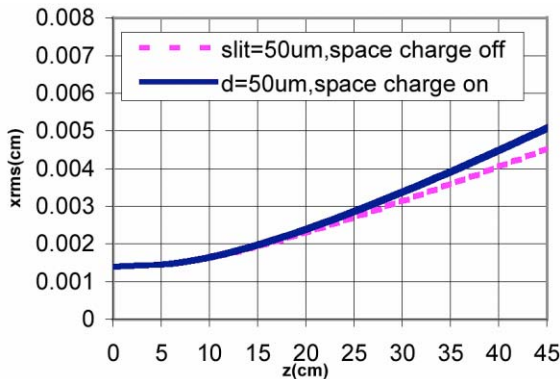


Figure 3: Analysis of the residual space charge effect after the metallic mask.

Every single slits are realized precisely machining a tungsten piece, and removing in the central part $50 \mu\text{m}$ of metal. Then the parts are stacked to build the multi-slits mask (see Fig.4) and two single slits mask $50 \mu\text{m}$ and $100 \mu\text{m}$ respectively. A prototype of the pepper-pot has been realized to verify the achievable machining accuracy for this design. In the first set of slits produced, 8 over 9 shown machining accuracy better than 10%, thus compatible with the needed tolerances. Since the multi-slits masks are made assembling single metallic parts,

they will be built selecting the best slits among those being produced. It is worth to mention that the precise values of the slit widths will be included into the analysis formula avoiding systematic errors in the evaluation of the beam emittance.

In the slits-array the distance between slits is $500 \mu\text{m}$ providing an adequate transverse sampling of the beam and compatibility with machining tools. The main advantage of a multi-slits mask is the possibility to have single-shot measurements, thus not affected by possible shot-to-shot beam fluctuations.

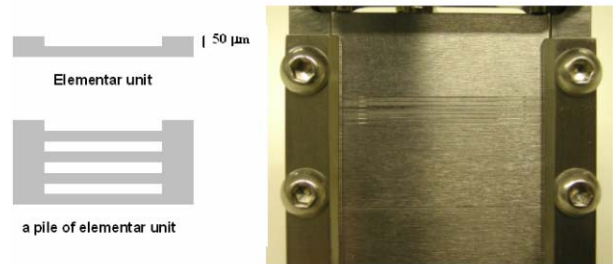


Figure 4: Slit mask design.

In spite of that, the multi-slits system might not be suited in such conditions where the beam is well focused and highly collimated, i.e. in the proximity of a beam waist, because the number of beamlets emerging from the multi-slit mask might not be sufficient for a good reconstruction of the phase space, as illustrated in Fig.5.

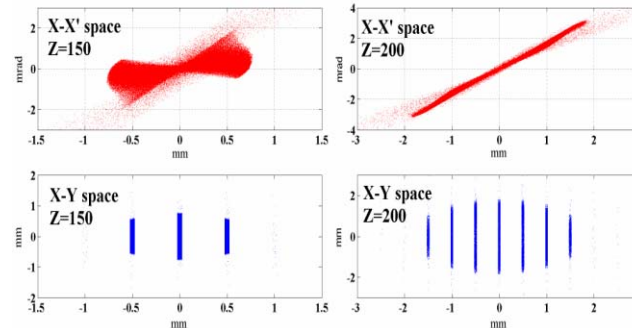


Figure 5: Phase space and multi-slit option for different scenario.

In this case we'll use a single slit to transversally scan the beam collecting together the image from different positions. In this case the measurement is not single shot and beam fluctuations must be taken into account.

The thickness (z-direction) of the slits defines the angular acceptance of the mask, i.e. the maximum divergence allowed for particle trajectories selected from the mask. As consequence, this value cannot be lower than the beam angular divergence otherwise the particles will be also selected because of their divergence and not just because their transverse position. Following a detailed analysis by simulations we decided to design the mechanical support in such a way to allow tilting of the metallic mask in order to optimize the mask vertical angle with respect to the beam before the measurements.

Screens and Image Acquisition

Two main requirements must be fulfilled by the radiator screen: it needs to have a linear response with beam charge in the range of few tenths of pC and it must guarantee a resolution better than 20 μm . Although OTR (Optical Transition Radiation) radiators, like aluminum foils, provide both high resolution and perfect linear response they have the disadvantage of a low intensity radiation. For our application, possible alternatives are Ce:YAG radiators and fluorescent material like BeO, that we are currently testing in the DAFNE Beam Test Facility.

For the image acquisition we'll use digital CCD cameras. They offer the advantage that the signal is digitalized directly from the camera electronics and there is no need of frame grabber, as result the outgoing signal, being it digital, will not be disturbed by the environmental noise. Furthermore the IEEE1394 (firewire) link allows simpler cabling topology because it carries both pixels readout and commands to the camera. A simple "macro" type objective will be used as imaging system.

Bellows

The influence on the beam quality of the 1.5 m long bellow has been investigated [3]. Wake fields perturbations due to the corrugated structure, especially when beam will not be well-aligned on-axis, were studied using HOMYDIN code and the wake fields were computed with the diffractive model Bane Sands.

The graph in Fig.6 shows the variation in percent of the beam emittance (at position $z=150$ cm from the cathode) due to a bellow misalignment for different values of the beam transverse position with respect to the bellow axis. In the worst case of 1 mm misalignment the contribution of the wakes to the emittance degradation is lower than 2%, thus practically negligible.

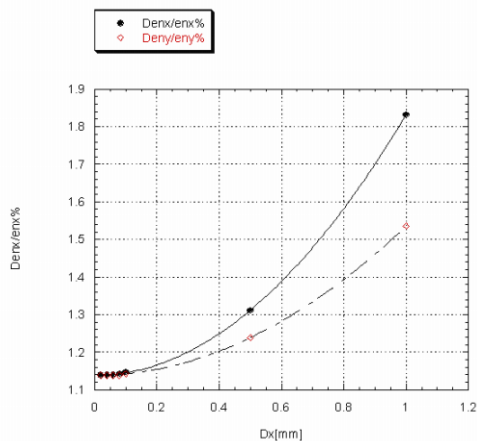


Figure 6: Degradation of the emittance due to a possible bellow misalignment.

The increasing of the energy spread due to the beam flight through the long bellows is analyzed in the plot of

Figure 7. As for the emittance, the degradation of the beam has not practical relevance.

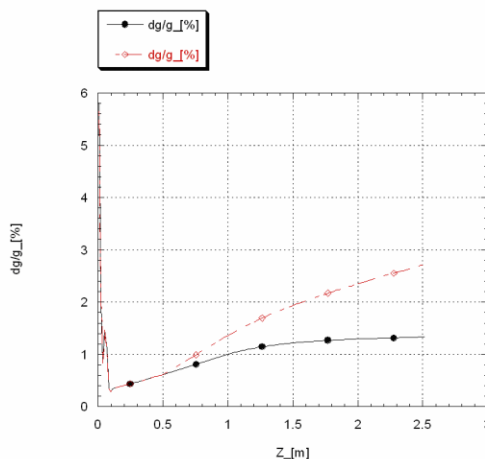


Figure 7: Energy spread vs z with (red curve) and without bellow.

CONCLUSION

The SPARC Emittance-meter will be built to perform a detailed study of the emittance compensation process in the SPARC photo-injector and to optimize the RF-gun and the accelerator working point. Installing the measurement system, based on the so-called "pepper-pot" method, between two long bellows we will have the possibility to scan a region 1.5 m long downstream the RF-gun.

Simulation codes have been used to study the layout and the mechanical design of the apparatus. Mask thickness, slits width, drift length between mask and screen, single slit vs. multi-slits option, alignment errors etc. have been studied to optimize the design and evaluate the performance of the system.

A prototype of the metallic mask has been already realized and measured. The overall apparatus design has been completed and the components are under construction at the LNF to be finally assembled by the end of 2004.

Acknowledgements

The authors want to acknowledge Valerio Lollo for his contribution to the design of the Emittance-meter.

REFERENCES

- [1] M. Zhang "Emittance Formula for Slits and Pepper-pot measurement", FERMILAB-TM-1998.
- [2] M. Boscolo, A. Cianchi, M. Ferrario, L. Picardi, M. Quattromini, C. Ronsivalle, J. Rosenzweig, "Status of the low-energy emittance measurement simulation for the SPARC project", SPARC-BD-03/005.
- [3] V. Fusco et al., "Wake Fields Effects in the Photoinjector of the SPARC Project", this proceedings.

AN RF DEFLECTOR DESIGN FOR 6D PHASE SPACE CHARACTERIZATION OF THE SPARC BEAM *

C. Vaccarezza, D. Alesini, LNF-INFN, Frascati, Italy;
M. Amadei, P. Casavola, A. Mostacci, L. Palumbo, Rome University La Sapienza, Roma, Italy;
J. Rosenzweig, UCLA, Los Angeles, CA, USA

Abstract

The characterization of the longitudinal and transverse phase space of the beam provided by the SPARC photoinjector is a crucial point to establish the performance quality of the photoinjector itself. By means of an RF deflector and a dispersive system, the six dimensional beam phase space can be analysed. A five-cell SW aluminum prototype of the SPARC RF deflector has been realized and tested. We report in this paper the design issues together with the RF measurement results. The simulation results of the 6D phase space reconstruction of the SPARC beam are also presented.

INTRODUCTION

The characterization of the longitudinal and transverse phase space of the beam at the exit of the third LINAC section, ($E \approx 150\text{MeV}$), is a tool to verify and tune the photoinjector performance. With a RF deflector it is possible to measure the bunch length and, together with a dispersive system, the longitudinal beam phase space can be reconstructed [1]. A schematic layout of the measurement is reported in Fig. 1. The effect of the RF deflector is null in the longitudinal center of the bunch and gives a linear transverse deflection to the bunch itself. If we consider the beam distribution and a drift space of length L after the deflector, the transverse kick results in a transverse displacement of the centroid of the bunch slice. The displacement is proportional to the slice longitudinal offset L_B , and RF voltage according to the expression:

$$x_B = \frac{\pi f_{RF} L L_B V_{\perp}}{cE/e} \quad (1)$$

where V_{\perp} is the peak transverse voltage, and E/e is the beam energy in eV units.

Equation (1) shows that the longitudinal bunch distribution can be obtained by measuring the transverse bunch distribution at the position z_s . To measure the bunch length with a proper accuracy, the “displacement” x_B has to be greater than the rms transverse beam size σ_x . The resolution length L_{res} can be defined, therefore, as the relative slice longitudinal position that gives, on the screen, an x_B equal to σ_x . From Eq. (1) we can calculate the transverse voltage V_{\perp} necessary to achieve the desired resolution:

$$V_{\perp} = \frac{\sigma_x c E / e}{\pi f_{RF} L L_{res}} \quad (2)$$

A voltage $V_{\perp} = 1.0\text{ MV}$ has been chosen for the RF deflector, obtaining a resolution of $\approx 2\%$. The complete longitudinal phase space measurement can be obtained adding the effect of a dispersive system. In this scenario, the bunch is vertically deflected by the RF deflector and horizontally by a magnetic dipole. The dispersion properties of the dipole allow characterizing the energy distribution of the bunch and the total longitudinal phase space can be displayed on the screen. The transverse phase space characterization is obtained measuring the beam slice emittance in both the transverse planes with the quadrupole scan technique.

SIMULATION RESULTS

A 150k particle beam obtained from PARMELA [2] simulation at the end of the linac section has been tracked with the ELEGANT code [3] along the SPARC transfer lines.

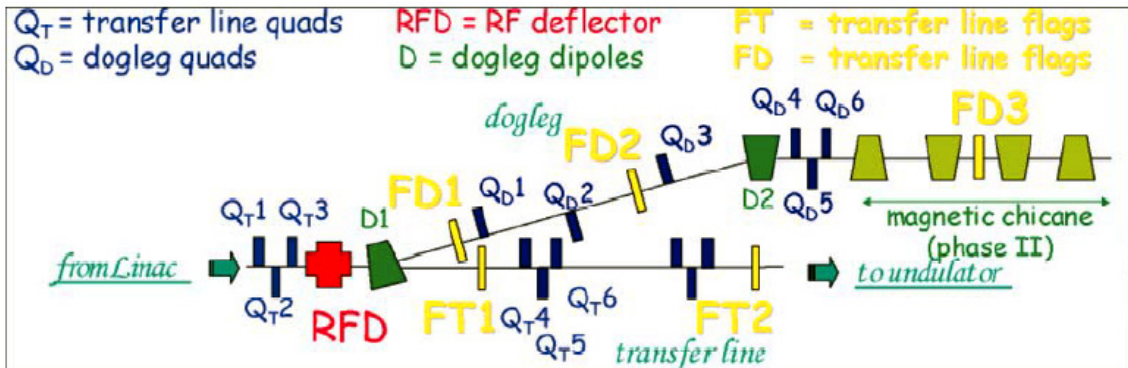


Figure 1: SPARC measurement layout for high energy beam characterization

The images of the beam obtained at the screen location, FT2, are shown in Fig. 2 with the RF voltage OFF and ON, respectively.

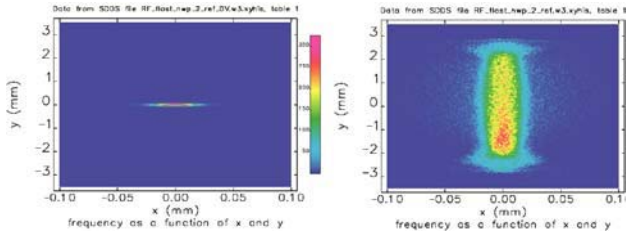


Figure 2: Bunch transverse distribution at the FT2 location with the RF deflector voltage OFF (left) and ON (right) respectively.

The results of the data analysis are shown in Fig. 3 where the vertical projected and the longitudinal distributions of the bunch are displayed.

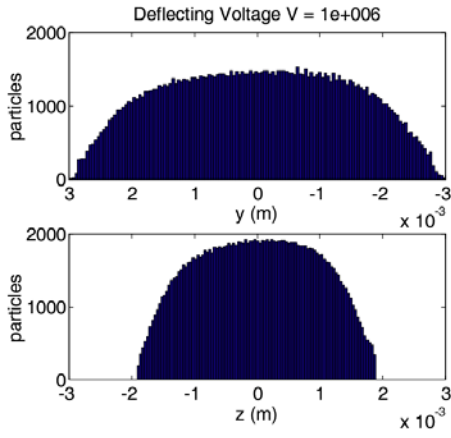


Figure 3: Above: the longitudinal bunch distribution as projected by the RF deflector on the vertical coordinate of the screen FT2; below: the particle distribution vs. time.

The value of σ_z , as obtained by applying Eq. (1), and by the longitudinal analysis of the raw data from ELEGANT tracking agree with an error less than 1%. The images collected on the dogleg at the screen located in FD2 show the reconstruction of the longitudinal phase space as shown in Fig. 4 where the time-energy ($z, \delta p/p$) distribution is replicated in the transverse plane (y, x).

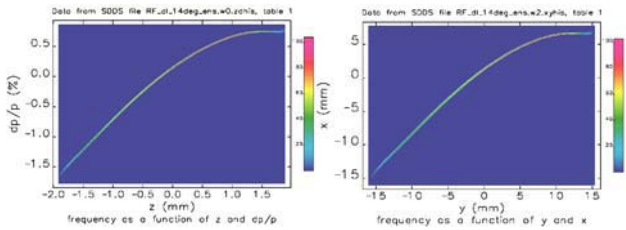


Figure 4: Above: Longitudinal phase space distribution of the SPARC beam. Below: Beam transverse distribution at the FD2 screen location as obtained tracking the beam through the SPARC dogleg with the RF deflector ON.

The “reconstructed” rms energy spread value is in very good agreement with the real one, and the same holds for the slice analysis. To measure the beam slice emittance in the horizontal plane the RF deflector is used to scan the beam rms size at the screen locations FT2.

In Fig. 5 the beam horizontal slice emittance is given for the simulated measurement: (left figure), on the right the result of the temporal analysis of the raw data is reported.

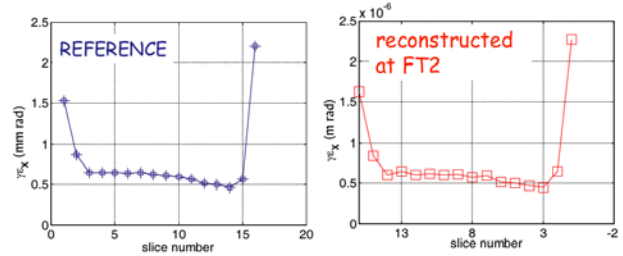


Figure 5: Reconstructed horizontal beam slice emittance (in mm-mrad) as a function of slice number with the beam size scanning at FT2. The left curve is the horizontal emittance as calculated by slicing the beam output file (tracked with Elegant) along the temporal coordinate, the right curve is the result of the simulated quadrupole scan at the screen location.

RF DEFLECTOR DESIGN

The simplest and more efficient multi-cell deflecting structure that can be used to deflect the bunch is a standing wave structure operating in the π -MODE. The choice of the number of cells has been done according to the following considerations:

- the available transverse deflecting voltage for a given input power;
- the available space in the SPARC transfer line;
- the mode separation with different number of cells to avoid problems of mode overlapping;
- the maximum acceptable surface peak electric field to avoid problems related to high field intensities, discharges and so on.

A 5-cell deflecting structure fulfils all of the stated requirements. In fact, it allows operating with a very low input power ($P_{RF} \leq 2\text{MW}$) obtaining contemporary low peak surface electric field and resolution length up to $\approx 25\mu\text{m}$. These characteristics permit measurement of the longitudinal beam profile with good accuracy, even considering the possibility of longitudinal compression factors of up to 20. Moreover the operation at low input power allows simplifying the power line design.

The 2D profile of the 5-cell RF deflector has been studied using the MAFIA 2D code. The simulated 5-cell profile is reported in Fig. 6 with the final dimensions and parameters shown in Table 1. The radius of the cells connected to the beam pipe tube in this design has been changed in order to achieve a field flatness of 3%. The on-axis magnetic field profile in the structure is plotted in Fig. 7.

Table 1: Final dimensions and parameters of the 5-cell deflecting structure.

Dimension [mm]	a	20.00
	$b_2=b_3$	59.97
	b_1	60.67
	t	9.50
	d	52.48
Param.	Frequency [GHz]	2.85699
	Q	16800
	R_{\perp} [$M\Omega$]	2.47

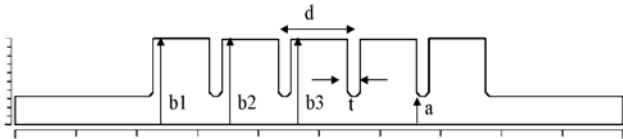


Figure 6: 5-cells deflecting cavity simulated by MAFIA2D.

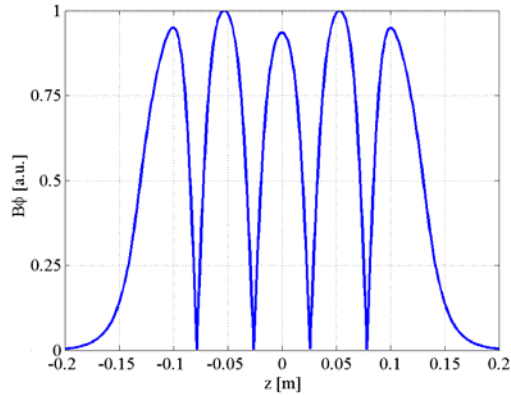


Figure 7: Absolute value of the magnetic field for the 5-cells cavity obtained by MAFIA 2D simulations.

The coupler design has been chosen to adapt a rectangular waveguide; more details about the design procedure can be found in [1].

PROTOTYPE MEASUREMENT RESULTS

A full-scale aluminum prototype, see Fig. 8, has been constructed to make field measurements and to implement tuning procedures. Bead-pull measurements have been done to measure the field flatness in the cavity [4]. Different perturbing objects have been used to measure the H-E field components. The tuning procedure that we have implemented is based on the study of field and frequency sensitivities with respect to the 5-tuners and is widely discussed in [5]. The reflection coefficient at the input coupler port is plotted in Fig. 9. The comparison between the measured quantities and the simulated ones is reported in Table 2. The external quality factor should be slightly increased by adjusting, experimentally, the window coupler dimensions.

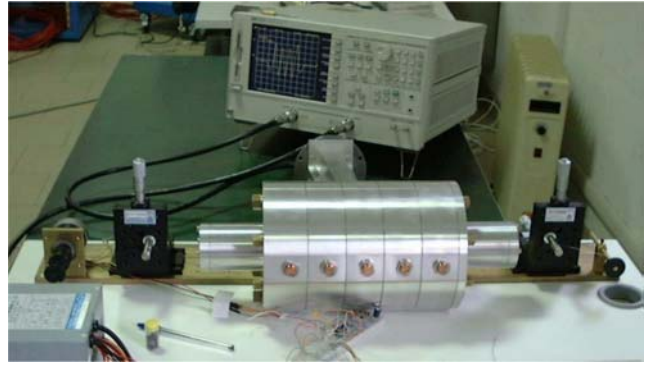


Figure 8: Deflector aluminum prototype and measurement setup.

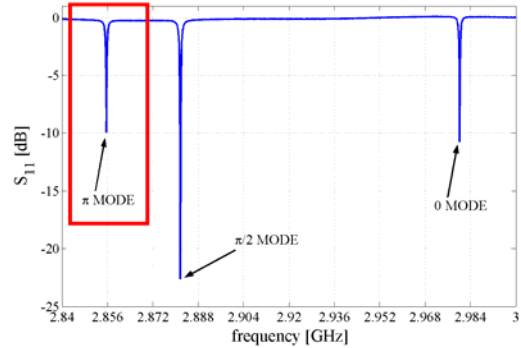


Figure 9: Measured reflection coefficient at the input coupler port.

Table 2: compare between the measured quantities and the simulated ones

	Q_0	Q_{EXT}	R_T/Q
Simulations	13200	16800	147
Measurements	6600	12900	149

CONCLUSIONS

A five-cell SW aluminum prototype of the SPARC RF deflector has been realized and test results are in agreement with the design predictions. The SPARC diagnostic layout has been presented together with the measurement simulation and the results of the 6D phase space reconstruction show the feasibility of a complete characterization of the longitudinal and transverse phase space of the beam provided by the SPARC photoinjector.

REFERENCES

- [1] D. Alesini and C. Vaccarezza, SPARC Note, SPARC-BD-03/001, Frascati, November 2003.
- [2] J. Billen, "PARMELA", LA-IUR-96-1835, 1996.
- [3] M. Borland, "Elegant: A Flexible SDDS-Compliant Code for Accelerator Simulation" LS-287, ANL,USA.
- [4] M. Amadei, Tesi di Laurea, Univ. of Rome "La Sapienza", 2003.
- [5] P. Casavola, Tesi di Laurea, Univ. of Rome "La Sapienza", 2004.

THE DESIGN OF A PROTOTYPE RF COMPRESSOR FOR HIGH BRIGHTNESS ELECTRON BEAMS

David Alesini⁺, Franco Alessandria^{*}, Alberto Bacci^{*}, Carlo De Martinis^{*}, Massimo Ferrario⁺,
Alessandro Gallo⁺, Dario Giove^{*}, Fabio Marcellini⁺, Marco Mauri^{*}, Luca Serafini^{*}

⁺INFN-LNF-Frascati, ^{*}INFN-Milan and University of Milan

Abstract

The generation of high brightness electron beams with longitudinal length less of 1 ps is a crucial requirement in the design of injectors for new machines like the X-ray FEL facilities. In the last years the proposal to use a slow wave RF structure as a linear compressor in this range of interest, to overcome the difficulties related to magnetic compressors, has been widely discussed in the accelerator physics community.

In this paper we will review the work carried out in the last 2 years and focused on the design a RF compressor based on a 3 GHz copper structure. The rationale of the conceptual design along with a description of the main experimental activities will be presented and a possible application of such a scheme to the SPARC project will be discussed.

INTRODUCTION

The strategy to attain high brightness electron beams delivered in short (sub picosecond) bunches is based on the use of RF Linacs in conjunction with RF laser driven photo-injectors and magnetic compressors. The formers are needed as sources of low emittance high charge beams with moderate currents, the latter are used to enhance the peak current of such beams up to the design value of 2-3 kA by reduction of the bunch length achieved at relativistic energies (> 300 MeV). Nevertheless problems inherent to magnetic compression such as momentum spread and transverse emittance dilution due to the bunch self-interaction via coherent synchrotron radiation have brought back the idea of bunching the beam with radio-frequency (rf) structures.

Such a type of bunching (named velocity bunching) has been experimentally observed in laser driven rf electron sources[1]. Velocity bunching relies on the phase slippage between the electrons and the rf wave that occurs during the acceleration of non ultra relativistic electrons.

It has been recently proposed to integrate the velocity bunching scheme in the next photoinjector designs using a dedicated rf structure downstream of the rf electron source [2]. The basic idea is to develop a rectilinear RF compressor, based on slow wave RF fields, that works indeed as a standard accelerating structure which simultaneously accelerates the beam and reduces its bunch length.

BASIC RF RECTILINEAR COMPRESSOR THEORY

The figure of merit for the compression may be defined as the ratio between the initial phase spread and the final one at the extraction. A simple model for the compression process may be developed analyzing the motion equations for an electron travelling in a rf structure. The phase extent at the extraction is a function of the initial energy spread and of the phase at the injection. A suitable tuning of the latter will result in an increase of the compression value.

A remarkable improvement of this scheme may be obtained whenever a beam, slower than the synchronous velocity, is injected into an rf structure at the zero acceleration phase, allowing it to slip back in phase up to the peak accelerating phase, and is extracted at the synchronous velocity.

A detailed mathematical treatment of this process may be found elsewhere [2]. The basic behaviour of the RF compressor may be easily understood thinking about an iris loaded TW structure designed to sustain a wave whose phase velocity is slightly lower than c (i.e. where

we have that $k = k_0 + \Delta k = \frac{\omega}{c} + \Delta k$ with the detuning

parameter. $\Delta k \ll k_0$). In such a structure the velocity of the beam will match that of the wave when the resonant beta and gamma can be well approximated by the

expressions: $\beta_r = 1 - \frac{c\Delta k}{\omega}$ and $\gamma_r = \sqrt{\frac{\omega}{2c\Delta k}}$, where

beta_r is the normalized phase velocity of the wave.

If beta_r is smaller than 1 the beam may advance in phase (i.e. slip forward on the wave) and the phase contour plots in the $[\gamma, \xi]$ phase space (ξ is the phase of the wave as seen by the beam) become closed curves. Figure 1 shows the phase compression picture achieved assuming the injection at $\xi=0$ and the extraction at $\gamma=\gamma_r$. The analytical expression for this phenomena becomes

$$\frac{1}{\gamma_r} - \alpha \cdot \cos(\xi_{ex}) = \gamma_0 - \beta_r \sqrt{\gamma_0^2 - 1} - \alpha \quad (1)$$

which shows that the extraction phase ξ_{ex} is a function of the injection conditions and the wave parameters. Using this expression it may be shown that compression values in excess of 9 may be obtainable and that the whole

compression process may be tunable in this range acting on the wave parameters.

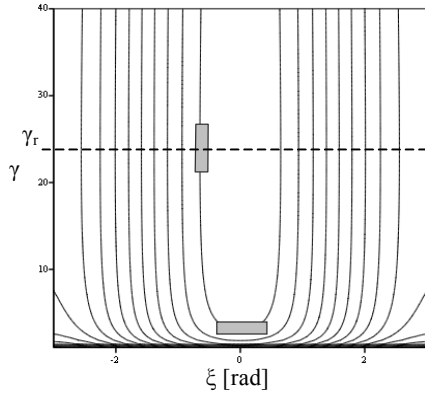


Fig. 1: Phase space plots of a slow RF wave

A PROTOTYPE SLOW WAVE RF COMPRESSOR

In 2003 we started a two years development program aimed at the design and construction of a slow wave TW structure which can be used as a prototype for a RF compressor.

The Italian SPARC injector project [3], whose target is the development of an ultra-brilliant beam photo injector for future SASE FEL based X ray sources, foresees the possibility to use a source like the one

above discussed and we used its parameters as a general reference to define the scientific case to study. Table 1 shows the main parameters which we used for our investigations:

Parameter	Value
Frequency of the wave structure	2856 MHz
Linac structure	TW
Accelerating gradient	20 MV/m
Initial energy	5.7 MeV
Extraction energy	14 MeV
Compression factor (at 130 MeV)	7
RF pulse repetition rate	1÷10
Bunch length	10 ps

Table 1: Reference parameters for the study of the RF compressor

The expression (1) shows that the rf structure parameter which provides the metric of the compression process in a slow wave structure is the phase velocity (v_f). In an iris loaded TW structure the phase velocity may be expressed as:

$$\frac{dv_f}{v_f} = \frac{df}{f} \cdot \left(1 - \frac{v_f}{v_g} \right)$$

The above relation shows that the v_f can be controlled by changing the excitation frequency or, in an equivalent way, by detuning the structure.

The first period of our study has been devoted to the

analysis of the way to detune in a controlled fashion the structure.

A preliminary analysis between possible alternatives showed that a thermal induced detuning of the rf structure, at a fixed exciting frequency, may be a suitable solution. The feasibility of this approach depends both on a detailed study of the compression factor as a function of the structure temperature and on a new design of the cooling system of the structure which takes into account all the requirements.

To investigate the effects of the temperature on the compression process we started evaluating the typical parameters of a standard SLAC structure. The required compression factor of 7 results in a change of the order of 1% of the phase velocity that is equivalent to a variation of the order of 0.6 °C in the temperature of the structure. This calls for a system able to control in real time the temperature set point with a resolution at least five times smaller (0.12 °C) both in term of sensibility and of stability. The RF power load on the structure, computed using the beam parameters of table 1, is of the order of 1.1 kW. The resolution required to the control system in such a situation was evaluated against the usual cooling plant specifications and in a survey of the available industrial components to be used as the building block of the new cooling facility. We evaluated that it would be too much difficult to achieve such a performance mainly due to the requirements in terms of stability. We decided to move toward a new TW structure designed to support slow waves and with the goal to decrease of a factor of 3 the thermal sensitivity, so that the required phase velocity modulation will ask for a temperature variation of the order of 2 °C. Table 2 shows the main parameters of the new structure (referenced as ALMA 5) which we propose for the RF compressor.

	SLAC Mark IV	Alma 5
Cell radius (mm)	41.24	42.48
Iris radius (mm)	11.30	15.40
Disk thickness (mm)	5.84	5.9
Cell length	35	35
Frequency (MHz)	2856	2856
Mode	2π/3	2π/3
Q	13200	13205
Shunt impedance (MOhm/m)	53	41
V_g/c	0.0122	0.0341
ΔT (equivalent to 1% V_f)	0.6 °C	2.0 °C
RF power required for a 3 meter long structure (MW)	-	66MW

Table 2: Main parameters of the Alma 5 TW structure

The group velocity has been increased of a factor of 3 to fulfil the requirement on thermal sensitivity. The subsequent decrease in shunt impedance has been considered acceptable since the maximum gradient required to the structure is lower than that of standard SLAC cavities. The last row in the table shows the power required to the Klystron that feeds the structure. This parameter has been carefully taken into account in the

design since, in principle, we may accept higher values of the group velocity (and consequently have a more comfortable thermal control) but this will result in an incompatibility with the RF power available for the SPARC project.

Using the parameters above reported a set of simulations have been carried out using codes as Homdyn and Astra to verify the behaviour of a full scale model composed of a slow wave structure followed by two standard SLAC cavities. The results have been plotted in fig. 2 and they show that the compression factor obtainable is at least a factor of two higher with respect to the result available using standard SLAC structures. The dependence of the compression factor on the thermal stability is of the order of 20% for 0.1 °C while for standard SLAC structures it is 3 times more.

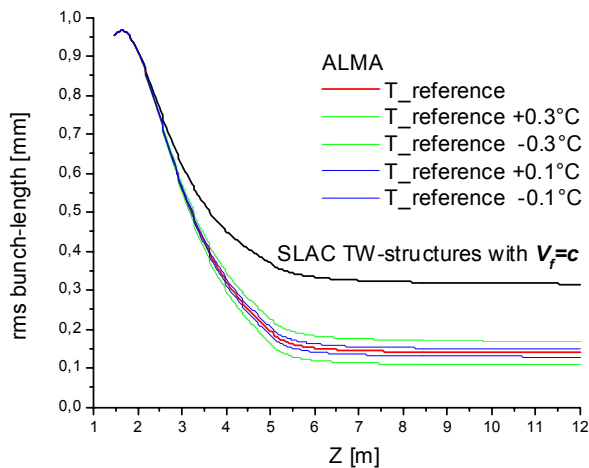


Fig.3: Simulations of the compression process

The mechanical design of the cell has been carried out taking into account the requirements due both to the brazing process and to the tuning. The results of the studies about the effects of the allowed machining tolerances have shown that a maximum error of 0.5° will be obtained. Such a value may be corrected using dinging holes, foreseen in the body of the cells, during the tuning process. Measurements carried out using aluminium based cells confirmed this predicted behaviour.

The thermal control of the structure has been studied using finite elements analysis. The solution has been found embedding the channels for water flow within the cells body to take advantage of the whole copper mass available. The cooling water will be provided to the structure by a Neslab HX300 compact cooling unit. This refrigeration unit has been chosen as the basic element around which build the cooling plant. It provides the capabilities to handle a maximum power load of the order of 10kW with a stability of the operating point of 0.1 °C.

To study the real behaviour of the cooling plant a test bench has been prepared using a 3 meter long standard SLAC cavity thermal controlled by the HX 300 unit. The cavity has been thermal insulated from the outside to reproduce as close as possible the characteristics of the ALMA 5 cooling circuits. The RF power load has been

simulated by a controlled resistive load. 20 temperature probes (Tc and RTD) have been installed on the cavity to measure the temperature in different points. A network analyzer measures in real time the resonant frequency of the structure which has been maintained under vacuum for the whole duration of the test.

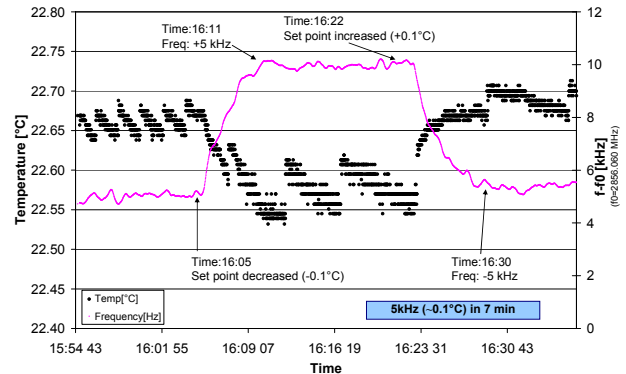


Fig.4: Temperature and frequency measurements

A significant measure is reported in fig. 4. The results show that the structure can be controlled with a stability better than 0.1 °C and that a change in the set point of the HX 300 controller of 0.1 °C is reflected in the structure within a few minutes. The RF behaviour of the structure is fully compliant with the simulations carried out using Superfish and Ansys.

CONCLUSIONS

The development of a prototype structure for a RF compressor is close to the final stage. The cell detailed design has been finished and it has been validated by preliminary tests on samples. A nine cells copper brazed structure will be available in August 2004 for an extensive set of measurements. The thermal control scheme has been defined and validated on a 3 meter long structure using the final components.

ACKNOWLEDGEMENTS

We would like to acknowledge very helpful discussions with S. Mathot (CERN) and the valuable support received in the experimental work by Luigi Gini (INFN-Milan) and Luciano Grilli (University of Milan). We also acknowledge J. Rosenzweig (UCLA) for the donation of the 3 m long SLAC structure used for the thermal tests.

REFERENCES

- [1] P.Piot "Subpicosecond Compression by Velocity Bunching in a Photoinjector", Physical Review, vol. 6 (2003)
- [2] L. Serafini et al. "Ultra-short Bunch Generation with a Rectilinear Compressor", PAC2001, Chicago, June 2001, p. 2242.
- [3] Sparc Collaboration "TDR for the Sparc Advanced Photoinjector" INFN-LNF rep., 12-1-2004

DESIGN STUDY FOR ADVANCED ACCELERATION EXPERIMENTS AND MONOCHROMATIC X-RAY PRODUCTION @ SPARC

D. Alesini, S. Bertolucci, M.E. Biagini, C. Biscari, R. Boni, M. Boscolo, M. Castellano, A. Clozza, G. Di Pirro, A. Drago, A. Esposito, M. Ferrario, V. Fusco, A. Gallo, A. Ghigo, S. Guiducci, M. Incurvati, C. Ligi, F. Marcellini, M. Migliorati, C. Milardi, A. Mostacci, L. Palumbo, L. Pellegrino, M. Preger, P. Raimondi, R. Ricci, C. Sanelli, M. Serio, F. Sgamma, B. Spataro, A. Stecchi, A. Stella, F. Tazzioli, C. Vaccarezza, M. Vescovi, C. Vicario, M. Zobov,

INFN-LNF, Frascati, Italy

F. Alessandria, A. Bacci, R. Bonifacio, I. Boscolo, F. Broggi, S. Cialdi, C. DeMartinis, D. Giove, C. Maroli, M. Mauri, V. Petrillo, N. Piovella, R. Pozzoli, M. Romè, L. Serafini,

INFN-MI and Univ. of Milano, Milano, Italy

U. Bottigli, B. Golosio, P. Oliva, A. Poggiu, S. Stumbo, *INFN/Cagliari and Univ. of Sassari, Italy*
A. Barbini, W. Baldeschi, C.A. Cecchetti, M. Galimberti, A. Giulietti, D. Giulietti, L.A. Gizzi, P. Koester, L. Labate, S. Laville, A. Rossi, P. Tomassini, *CNR-IPCF/Pisa and Univ. of Pisa, Italy*

Abstract

We present a design study for an upgrade of the SPARC photo-injector system, whose main aim is the construction of an advanced beam test facility for conducting experiments on high gradient plasma acceleration and for the generation of monochromatic X-ray beams to be used for applications like advanced medical diagnostics and condensed matter physics studies. Main components of the proposed plan of upgrade are: an additional beam line with interaction regions for synchronized high brightness electron and high intensity photon beams (co-propagating in plasmas or counter-propagating in vacuum) and the upgrade of the SPARC Ti:Sa laser system to reach pulse energies in excess of 1 J. Results of numerical simulations modelling the beam dynamics of ultra-short bunch production, based on a slit-selection technique combined with double RF deflection, are presented. Calculations of the monochromatic X-ray beam angular and frequency spectra, generated via Thomson back-scattering of the SPARC electron beam with the counter-propagating laser beam, are also presented. X-ray energies are tunable in the range 20 to 500 keV, with pulse duration from sub-ps to 20 ps. The proposed time schedule for this initiative, tightly correlated with the progress of the SPARC project, is finally shown.

INTRODUCTION

The SPARC photo-injector under installation at INFN-LNF will provide an ultra-bright electron beam at 150 MeV kinetic energy for the investigation of a SASE-FEL experiment, as extensively described elsewhere [1]. The beam is expected to be delivered in bunches of up to 1.1 nC of charge, rms normalized projected emittance smaller than 2 mm·mrad, rms energy spread smaller than 0.2 % with rms bunch length of about 2-3 ps (uncompressed beam). The electron bunches will exit the photo-injector with 1 ps time jitter w.r.t. laser pulses: these are produced

by a synchronized mode-locked Ti:Sa laser system delivering 20 mJ pulses in the IR (800 nm) at 10 Hz repetition rate, which are converted to UV (266 nm) to drive the electron beam production by hitting a photocathode located inside a RF gun. The foreseen availability of a bright electron beam and an intense synchronized laser is an ideal combination to pursue experiments by exploiting the interaction of the two beams (electrons and photons) either co-propagating or colliding them. High gradient plasma acceleration or mono-chromatic bright X-ray beam production in Thomson sources are noticeable examples of these beam interactions. For both of them a TW peak power laser beam and ultra-short (sub-ps) electron bunches are required. An upgrade of SPARC aimed at addressing these issues must conceive the development of 3 key components: the laser must be further amplified to reach the level of a few Joule of energy per pulse, the photo-injector has to be provided with an additional transport beam line to serve the interaction region, a dedicated diagnostic and control system has to be developed to operate the beam interaction efficiently. The Ti:Sa SPARC laser system will be installed starting this fall: it will comprise a diode-pumped 150 fs oscillator, a solid-state pumped regenerative amplifier (2 mJ) and a flash-pumped multi-pass amplifier (20 mJ). We foresee to upgrade the laser in two steps: a first multi-pass amplifier to reach the level of 200 mJ energy per pulse with in air compressor down to 100-200 fs pulse length, and a second multi-pass amplifying stage, to reach the 1-3 J energy per pulse, equipped with in vacuum compressor to hold the 10-30 TW peak power delivered at this final stage. Since the specified time jitter for the SPARC laser system is smaller than 1 ps (with 0.5 being the desired value), we can foresee to achieve the correct space-time overlap of the colliding electron and laser pulses in the final focus region of the Thomson source for monochromatic X-ray production as far as the electron bunch is

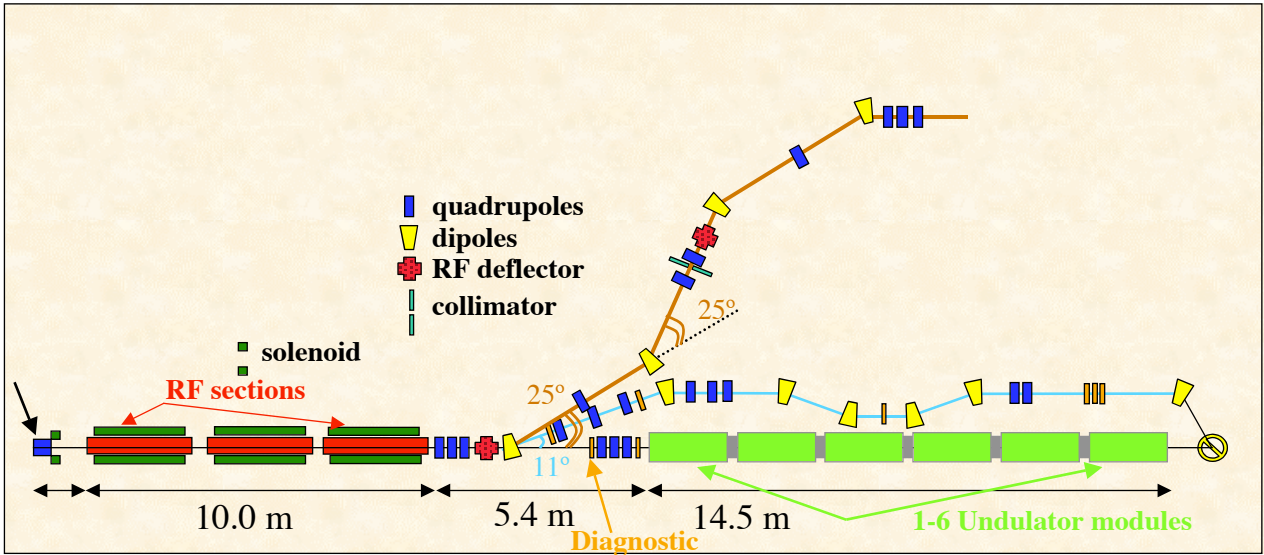


Figure 1: Lay-out of SPARC photo-injector and SASE-FEL experiment with additional double dog-leg beam line

the standard uncompressed beam delivered by the SPARC photo-injector (2-6 ps rms bunch length). For the interaction of ultra-short pulses (rms length smaller than 0.5 ps) we need to improve the synchronization level between the two beams. The anticipated beams that we aim to deliver with the SPARC advanced beam facility are listed in Table 1, which contains the main beam parameters of interest, like bunch charge, kinetic energy, rms bunch length, normalized transverse emittance and energy spread (numbers in bold mark the most critical beam parameter for the specific application). The FEL-SASE application requires a very small emittance beam with peak current in excess of 100 A (hence the 1 nC bunch charge at a few ps rms bunch length), the plasma acceleration experiment (exploited by sending the laser into a gas jet to drive a plasma wave in a synchronized fashion to the ultra-short electron bunch injected in phase into the plasma wave for further acceleration) needs ultra-short bunches, while the Thomson source needs very small energy spread beams to avoid chromatic aberrations in the final focus system where the beam is focused down to sub-10 μm spot sizes to collide with the laser beam.

Application	Q (nC)	T (MeV)	σ_t (ps)	ϵ_n (μm)	σ_y/γ (%)
FEL-SASE	1	150	3	2	0.1
Plasma-Acc.	0.025	100	0.025	0.1	0.2
X-Thomson	1	30-150	6-3	2	0.05-0.2

Table 1: anticipated beams @ SPARC

TRANSPORT BEAM LINE

The lay-out of the SPARC photo-injector with additional transport beam line is plotted in Fig.1: the 3 linac sections, embedded in solenoids, launch the beam

through a triplet, followed by the first RF deflector, a double bend dog-leg containing a beam collimator (a slit in the beam vertical plane) and the second RF deflector, taking the beam into a final quadrupole triplet to apply final focusing in the interaction region. While the beam for the Thomson source is transported unchanged through the dog-leg, the ultra-short bunch is produced by properly selecting a thin slice (25 μm) of the SASE-FEL beam produced at 150 MeV by the SPARC photo-injector. The slice selection is accomplished as follows: the first RF deflector induces a correlation between vertical position of each bunch slice at the slit position (located at the symmetric plane of the double dog-leg) and its longitudinal coordinate within the bunch, the slit clips a specific slice, finally the second RF deflector removes the time-z correlation imparted by the first deflector. It should be noticed that this technique is somewhat similar to the one proposed[2] for LCLS with the aim to generate fs long electron bunches, but it differs from that in the use of RF deflectors, which remove the need of correlated energy spread (energy vs. slice position within the bunch).

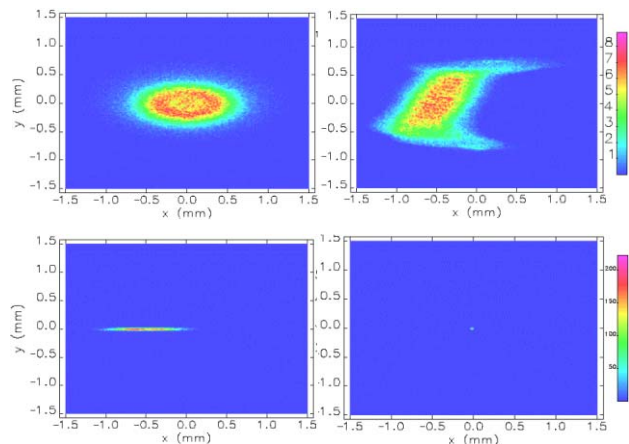


Fig. 2: beam distribution in (x,y) along the beam line

The beam density distribution in the transverse (x,y) plane is plotted in Fig.2, at 4 different positions along the beam line, *i.e.* at the photo-injector exit (upper left diagram), after the first RF deflector (upper right), after the slit (lower left) and after the second RF deflector and the final focusing triplet: the focal spot sizes are 7 and 2 μm (in x and y respectively) while the bunch rms length is 25 μm (25 pC of bunch charge selected through the slit, simulations performed with PARMELA and ELEGANT). The longitudinal phase spaces are shown in Fig.3.

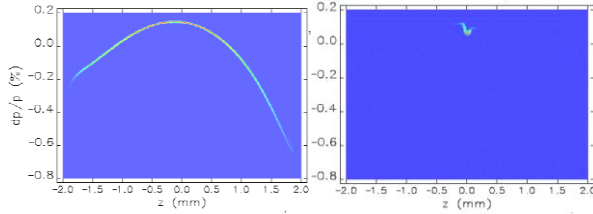


Fig. 3: beam distribution in $(\delta z, \delta p/p)$ before and after the double dog-leg with 2 RF deflectors and slit

THOMSON SOURCE

The collision of a relativistic electron beam and a powerful laser gives rise to X-ray photons generated via the Thomson back-scattering effect (when the energy of the emitted photon is much smaller than the electron rest mass energy, *i.e.* recoil effects are negligible). The energy w_x of the emitted X-ray photon is given by

$w_x = w_{las} \left(1 - \beta \cos \alpha_l / 1 - \beta \cos \vartheta_{ob} \right)$, where w_{las} is the laser photon energy (1.5 eV for our case), α_l is the colliding angle and ϑ_{ob} the observation angle. Head-on collisions ($\alpha_l = \pi$) observed on axis ($\vartheta_{ob} = 0$) give rise

to X-ray photons of energy $w_x = 4\gamma^2 w_{las}$. A relevant range of energy is around 20 keV, in particular for advanced clinical diagnostics applications. Applying head-on collisions, which maximize the X-ray beam flux, it turns out that the electron beam energy must be 30 MeV, much smaller than the nominal SPARC value for which the photo-injector has been designed. Therefore, we had to derive a different operating point for the photo-injector, based on the launch of a longer bunch at the photo-cathode (30 ps laser pulse length, 1 nC, cathode spot size 0.6 mm) at lower phases, which generates a 20 ps electron bunch at the gun exit due to a weak bunching effect in the gun. The beam is accelerated by the first linac section up to 30 MeV, the second linac section is run at zero phase to remove the correlated energy spread while the third section is turned off. The combined effects of longitudinal wake-fields and a 4th harmonic X-band cavity are used to correct the longitudinal emittance by removing the RF curvature, thus achieving a final rms

energy spread lower than 0.05%. The transverse and longitudinal beam dynamics through the photo-injector are shown in Fig. 4 and Fig.5, respectively (simulations performed with ASTRA). A final lens focuses down the 30 MeV beam to a 10 μm spot size at the collision point.

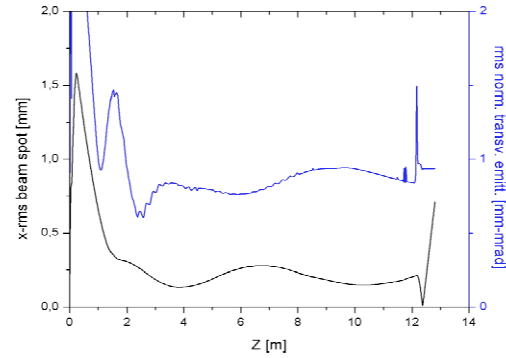


Fig. 4: 30 MeV beam for Thomson source: transv. dyn.

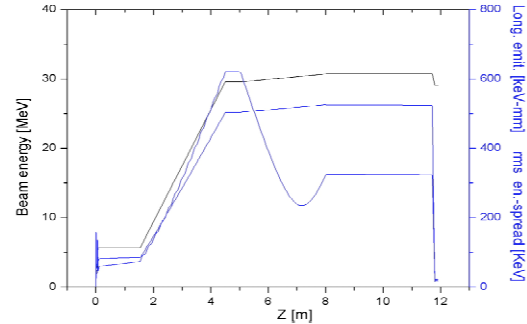


Fig. 5: 30 MeV beam for Thomson source: longit. dyn.

The estimated energy spectrum of the X-ray beam generated by colliding the electron beam with a 3 J laser pulse, 3 ps long and focused down to a spot size of 20 μm , is shown in Fig. 6. $2 \cdot 10^8$ X-ray photons per collision are produced with 5% rms energy spread within a solid angle defined by $\vartheta_{ob} = \pm 6 \text{ mrad}$.

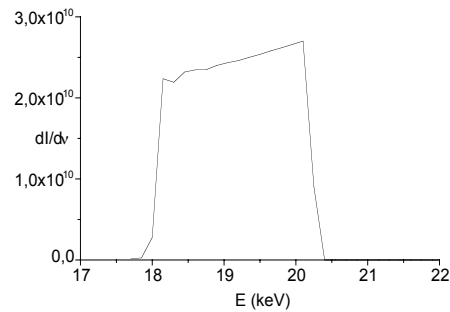


Fig. 6: X-ray beam energy spectrum

REFERENCES

- [1] D. Alesini et al., "Status of the SPARC Project", this conference, see also D. Alesini et al., in publication on *NIM-A* 21566
- [2] P. Emma et al., *Phys. Rev. Lett.* **92**, 074801-4.

AN ULTRA-HIGH BRIGHTNESS, HIGH DUTY FACTOR, SUPERCONDUCTING RF PHOTOINJECTOR

M. Ferrario, INFN-LNF, Frascati (Roma), Italy
J.B. Rosenzweig, G. Travish, UCLA, Los Angeles (CA), USA
J. Sekutowicz, W.D. Möller DESY, Hamburg, Germany

Abstract

Recent advances in superconducting rf technology and a better understanding of rf photoinjector design make possible to propose a superconducting rf gun producing beams with ultra-high peak brightness and high average current. The superconducting rf photoinjector presented here providing such high quality beam is scaled from the present state-of-the-art design of the normal conducting rf photoinjector that has been studied for LCLS SASE FEL.

INTRODUCTION

With the advent of proposed [1, 2] superconducting radio-frequency (SRF) electron linear accelerators dedicated to production of radiation or to high energy physics that operate at high average current (high duty factor), the demand for high quality beams, *i.e.* high peak brightness*, pushes one to consider the possibility of using a SRF photoinjector. Usually, to enhance brightness one has to expose emitting cathode to a very high electric field, and also to introduce magnetic solenoid fields within the photoinjector gun region. These focusing fields allow control and mitigation of space-charge effects, a process termed emittance compensation. Operation with high average beam current requires photocathodes having enhanced quantum efficiency (η). When superconductor is used as a photoemitter, high η minimizes the thermal load on the superconducting surface. More generally, high η implies that one may keep the size and cost of the high duty cycle laser system used to illuminate the photocathode within reasonable limits.

In the past, for an implementation of SRF guns it was always assumed that one needs strong focusing inside the gun, near the photocathode. This assumption has been partially driven by relatively low achievable gradient in SRF guns in the past. An interesting solution which avoids use of solenoid fields in transverse beam control near the cathode, so-called “rf focusing”, has been proposed in [3]. Unfortunately this method requires a deformation of the cathode plane, causing nonlinear field perturbations that may cause significant emittance growth in the injector. We discuss in the following sections an alternative scheme in which rf focusing is not required. This optimized SRF gun is based on the scaling of existing normal conducting high brightness sources to lower frequency and lower rf field.

* Peak Brightness: $B = 2I_p / \varepsilon_n^2$ where I_p is the peak current and ε_n is the normalized transverse emittance.

Concerning the choice of the cathode material, it has been shown experimentally [11] that with various treatments of a Nb surface (mechanical diamond polishing or/and laser polishing), one can increase the Nb η from $2 \cdot 10^{-7}$ to $5 \cdot 10^{-5}$. Further increase of η is possible when emitting spot is exposed to high electric fields, through the Schottky effect. Since η scales proportional with electric field applied at the emitting spot one may expect that at gradients of 60 MV/m quantum efficiency will increase to 10^{-4} , or above if higher energy photons can be used to illuminate Nb wall. An improvement in η is of great importance. Even with $\eta = 10^{-4}$ the laser-deposited power in the Nb wall needed accompanying cw, few MHz 1 nC/bunch beam photoemission, would be too high to keep the illuminated spot superconducting [12]. In addition, the illuminating laser itself would be technically very challenging.

More recently, a new approach to the generation of high-current, high-brightness electron beams has been proposed by the BNL group [4]. In this scheme, primary electrons are produced by a photocathode and are accelerated to several keV. At that energy they strike a specially prepared diamond window. The large secondary electron yield (SEY) of diamond multiplies the number of secondary electrons by about two orders of magnitude. These electrons drift through the diamond under an electric field and emerge into the rf accelerating field in the gun through the diamond’s negative electron affinity surface. The advantages of this approach are evident in the context of SRF photoinjectors.

BASIC DESIGN PARAMETERS

It is often remarked that production of a very high brightness beam from an rf photoinjector implies the use of a large accelerating gradient. For example, the design for the LCLS photoinjector, which is presently the highest brightness source proposed, utilizes a peak on-axis electric field of between 120 and 140 MV/m at an operating rf frequency of 2.856 GHz [5]. While such fields clearly exceed those achievable in superconducting rf cavities, one may easily scale the fields downward by moving to a different design frequency [6]. As the longitudinal beam dynamics are preserved in this case by scaling the fields as $E_0 \propto \lambda_{rf}^{-1}$, at L-band (1.3 GHz) the needed peak on-axis field is between 54 and 64 MV/m, which is roughly equivalent to an average accelerating field between 27 and 32 MV/m. These fields are within the current state-of-the-art in superconducting cavities [7].

The working point of the LCLS photoinjector is predicted to have a very high brightness, with a peak current at 1 nC charge of 100 A (10 psec flat-top pulse), and an emittance of 0.7 mm-mrad [8]. With these beam parameters, obtained from detailed PARMELA simulation, the calculated B is $5.6 \cdot 10^{14}$ A/m². One may scale the space-charge dominated beam dynamics naturally and exactly in rf wavelength, scaling the beam dimensions by the rf wavelength $\sigma_i \propto \lambda_{rf}$ the solenoid field as $B_z \propto \lambda_{rf}^{-1}$, and the beam charge by $Q \propto \lambda_{rf}$ [6]. Under these assumptions, the current is independent of λ_{rf} , and the emittance scales as λ_{rf} —thus the brightness scales as $B \propto \lambda_{rf}^{-2}$. Fortunately, if we scale back the charge at L-band from 2.2 nC (natural scaling), to 1 nC, we do not pay a strong penalty in brightness. For scaling of charge, we must keep the beam plasma frequency constant, which requires that $\sigma_i \propto Q^{1/3}$. Under these conditions of both charge and wavelength scaling, it can be shown that the brightness scales as

$$B(\text{A/m}^2) = \frac{2 \times 10^{12}}{a_1 \lambda_{rf}^2 (m) + a_2 Q^{4/3} (\text{nC}) \lambda_{rf}^{2/3} (m) + a_3 Q^2 (\text{nC})}$$

where the constants a_i are deduced from simulation scans. These constants have physical meaning: a_1 indicates the contribution of thermal emittance; a_2 the component due to space charge; a_3 the emittance arising from RF and chromatic effects. For the LCLS design "family" [9], these constants are determined to be $a_1 = 1.5$, $a_2 = 0.81$, $a_3 = 0.052$.

For our L-band scaled design at 1 nC charge, we obtain a current of 50 A, and an emittance, as before, of 0.7 mm-mrad, for a peak brightness of $B = 2 \times 10^{14}$ A/m² which we expect from a potentially very high brightness superconducting source. The possibility is thus within reach that a scaled SRF version of the LCLS injector may give bunches of electrons with extremely high brightness,

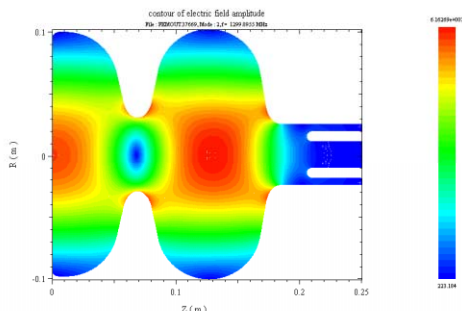


Figure 2: 1.3 GHz 1.6 cell Nb SRF gun design

at average repetition rates well in excess of the present state of the art.

SRF CAVITY AND SOLENOID DESIGN

The proposed 1.3 GHz 1.6 cell Nb cavity, used here to design the injector is shown in Fig. 2. The full cell dimensions are the similar to an inner cell of a TESLA cavity, while the first cell is longer than a half cell ($0.6 \lambda_{rf}/2$) in order to compensate for phase slippage occurring during the early, non-relativistic phase of beam acceleration. A coaxial input power coupler has been considered as in the normal conducting TESLA gun design [1], in order to avoid any asymmetry in the accelerating field and transverse RF kicks. The HOM coupler is located on the beam tube close to full cell iris.

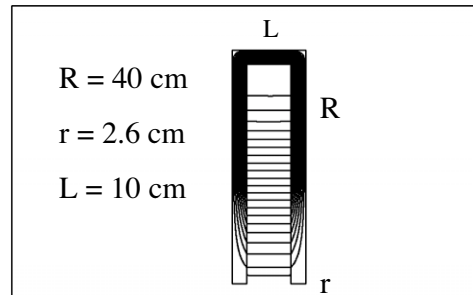


Figure 3: design of the solenoid coils

Further, this nearly scaled configuration has a focusing solenoid geometry that keeps most of the magnetic field outside the cavity. In fact in the frequency-scaled, superconducting case, we have further constraints. The magnetic field must not penetrate the superconducting cavity to avoid thermal breaks down when the critical field of 200 mT is exceeded. The residual fringing field (4 Gauss on the cavity iris see Fig. 4) is tolerable in that the focusing is applied only after cool down and the small field is excluded from the superconducting cavity through the Meissner effect, thus avoiding any residual flux trapping that may cause cavity Q_0 degradation. In Fig. 3 a schematic design of the solenoid coils and iron screen is shown and in Fig. 4 the on-axis E_z component of the RF field and solenoid B_z are displayed.

A more detailed study including the laser system and cryostat design will be discussed in a future work.

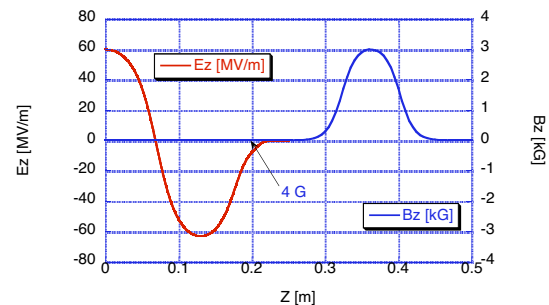


Figure 4: On-axis profiles of the RF field E_z , and B_z

BEAM DYNAMICS SIMULATIONS

PARMELA simulations performed with 50,000 macroparticles are shown in Fig. 5 and 6 up to the 1 mm-mrad emittance threshold. Longer distances have been studied by the fast running code HOMDYN and the results are shown in Fig 7.

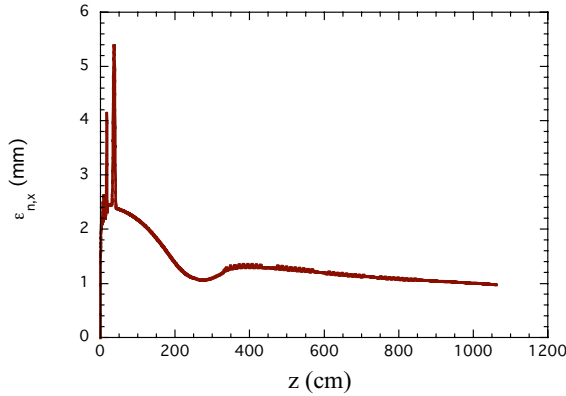


Figure 5: Rms normalized emittance evolution in SC photoinjector, from PARMELA simulations

According to the scaling philosophy discussed in the previous section, in our simulation we consider a uniform density 1 nC bunch 19.8 ps long and radius of 1.69 mm, accelerated in the gun cavity up to an energy of 6.5 MeV, corresponding to a peak field on the cathode of 60 MV/m and an injection phase of 44.5 deg. Space charge induced beam expansion (up to $\sigma_x=2.4$ mm) and emittance growth in the gun are compensated in a downstream drift with a solenoid located at the gun exit, 36 cm from the cathode, producing a 3 kG maximum field on the axis.

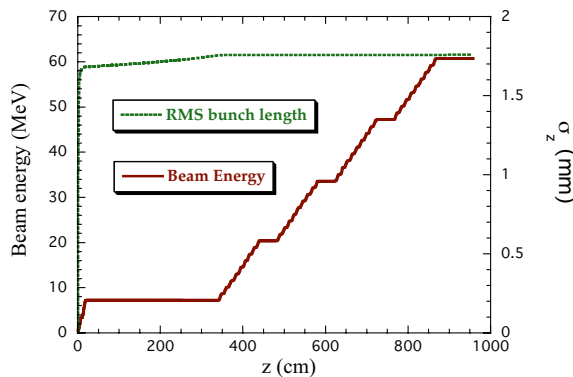


Figure 6: Rms bunch length and energy evolution, in SC photoinjector, from PARMELA simulations.

As shown in Fig. 5 the emittance compensation process is clearly visible in the drift until the bunch is injected at $z=3.3$ m in a cryomodule housing 8 L-band superconducting cavities of the TESLA type. Matching conditions for optimum emittance compensation [10] sets the accelerating gradient to 13 MV/m. At the exit of the first cryomodule ($z=14$ m) the bunch has been accelerated up to 117 MeV (the beam is space charge dominated up to 90 MeV) and space charge induced emittance oscillations

are totally damped (see Fig. 7). The final emittance is lower than 1 mm-mrad (with a thermal emittance contribution of 0.5 mm-mrad). A minor bunch elongation (see Fig 6.) in the drift results in a final peak current of 50 A. The total length of the injector system is 14 m.

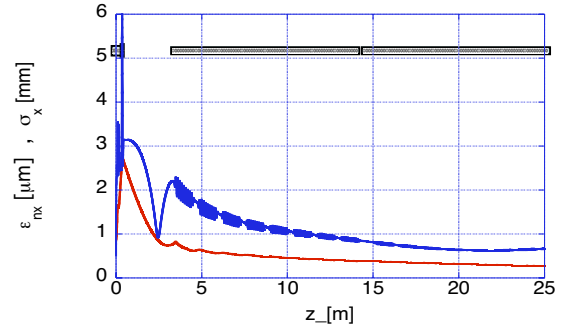


Figure 7: Rms normalized emittance and rms envelope evolution up to the exit of the second cryomodule, HOMDYN simulations.

REFERENCES

- [1] H. Weise, "The TESLA X-FEL project", this conference
- [2] J. Sekutowicz et al., "Proposed Continuous Wave Energy Recovery Operation of an XFEL", TESLA-FEL Report 2004-03, submitted to PRST-AB.
- [3] D. Janssen, V. Volkov, Nucl. Instr. and Meth. A 452 (2000), 34.
- [4] I. Ben-Zvi et al., "Secondary Emission Enhanced Photoinjector", BNL Report C-A/AP/#149
- [5] D. Dowell et al, "The Linac Coherent Light Source Photo-Injector", this conference
- [6] J.B. Rosenzweig and E. Colby, "Charge and Wavelength Scaling of RF Photoinjector Designs", *Advanced Accelerator Concepts* p. 724 (AIP Conf. Proc. 335, 1995).
- [7] L. Lilje, "Achievement of 35 MV/m in the TESLA Superconducting Cavities Using Electropolishing as a Surface Treatment", this conference
- [8] M. Ferrario et al., "HOMDYN study for the LCLS Photoinjector", in *The Physics of High Brightness Beams*, 534, World Scientific, 2000.
- [9] M. Biagini et al., "SPARC Photoinjector Working Point Optimization, Tolerances and Sensitivity to Errors", this conference
- [10] L. Serafini, J. B. Rosenzweig, Phys. Rev. E **55** (1997) 7565
- [11] T. Srinivasan-Rao et al., "Design, Construction and Status of All Niobium Superconducting Photoinjector at BNL", PAC03, Portland 2003, USA
- [12] T. Schultheiss et al., "Thermal/Structural analysis of a SCRF Photocathode Electron Gun Cavity", PAC01, Chicago 2001, USA.